12-2011

Aeolian Simulations: A Comparison of Numerical and Experimental Results, with Projections for Titan.

Oscar Lee Mathews
omathew1@utk.edu

To the Graduate Council:

I am submitting herewith a thesis written by Oscar Lee Mathews entitled "Aeolian Simulations: A Comparison of Numerical and Experimental Results, with Projections for Titan.." I have examined the final electronic copy of this thesis for form and content and recommend that it be accepted in partial fulfillment of the requirements for the degree of Master of Science, with a major in Aerospace Engineering.

James E. Lyne, Major Professor

We have read this thesis and recommend its acceptance:

Devon Burr, Zhili Zhang

Accepted for the Council:
Carolyn R. Hodges

Vice Provost and Dean of the Graduate School

(Original signatures are on file with official student records.)

Aeolian Simulations: A Comparison of Numerical and Experimental Results, with Projections for Titan.

A Thesis
Presented for the
Master of Science
Degree
The University of Tennessee, Knoxville

Oscar Lee Mathews
December 2011

Dedication

To my family: my parents David and Pilar Mathews, and my sibling, Anthony Mathews. Thank you all for encouraging me, and helping me to continue to believe that all things are possible.

Acknowledgments

This author would like to dedicate this work to his teachers, professors and military leaders who have made him who he is today; they deserve his thanks and heart-felt appreciation. Thanks also go out to the Titan Research Team and John Hills for his efforts, which contributed in part to this thesis. The author would also like to acknowledge the collaboration of Jasper Kok, with whom many productive discussions were had. The many friends who edited and commented on this thesis deserve special recognition, and made the final work presented much more enjoyable to read.

Abstract

Aeolian processes are major determinants of geomorphology on bodies in the Solar System possessing an atmosphere-surface interface and transportable sediment, including Earth, Mars, Venus, and Titan. Substantial efforts have been made over the last few decades to understand these processes using specialized wind tunnels, field studies, and, more recently, numerical simulations. This thesis describes a model of aeolian sediment transport using computational fluid dynamics (CFD), and compares the results with those obtained in the Martian Surface Wind Tunnel (MARSWIT) testing conducted in the Planetary Aeolian Laboratory at NASA Ames Research Center. The ultimate goal of the thesis was to develop an experimentally validated computational approach for modeling aeolian sediment saltation on Titan and other planetary bodies.

In this thesis, sieved walnut shell particles with diameters of 175-250 microns were placed on the test section floor of the MARSWIT tunnel, the tunnel was started, and the free stream airspeed was raised to ~2.5 to 7.5 m/s. A Phantom v12 high-speed camera was used to image the resulting particle motion at 1000 frames per second, and the open source software, ImageJ, was used to evaluate particle motion.

Airflow in the MARSWIT facility was modeled with Ansys FLUENT, a commercial CFD program. Surface properties for roughness height (K_s) and roughness constant (C_s) were determined through computation of a dimensionless roughness height parameter, K_S^+, while using von Kármán's constant. The turbulent scheme used in FLUENT to obtain closed-form solutions to the Navier-Stokes equations was a 1st Order Discretization, k-epsilon (two-equation) model. These methods produced computational velocity profiles that agreed with experimental data to within 10-15%. Once satisfactory modeling of the flow field had been achieved, a Discrete Phase Model (DPM) was utilized to simulate particle trajectories numerically. A Euler-Lagrangian scheme was employed, treating the particles as spheres and tracking each particle at its center. Calculated particle trajectories agreed closely with experimental results, within error bounds. Projections of Titan trajectories for specific conditions are among the major results presented and discussed and show higher and longer lofts than currently estimated.

Contents

1 Introduction…… 1

1.1 Overview and Purpose of this Thesis…… 1

1.2 History and Current State of Aeolian Transport…… 3

1.3 The Case for CFD Modeling of Aeolian Transport…… 3

1.4 Section Summary…… 5

2 Background…… 6

2.1 Summer Research at NASA Ames…… 6

2.2 MARSWIT Wind Tunnel Specifications at NASA Ames …… 7

2.3 American Geophysical Union (AGU) Fall Meeting…….. 8

3 Overview of Theoretical Principles and Mechanics…… 9

3.1 Overview of Fluid Mechanics Principles…… 9

3.1.1 Navier-Stokes Equations…… 9

3.1.2 Robins-Magnus Force Effect……. 11

3.1.3 Particle Drag ……. 14

3.1.4 Boundary Layer and Velocity Profile…… 15

3.1.5 Knudsen Number…… 17

3.1.6 Hydraulic Diameter…… 18

3.1.7 Turbulence Length Scales……. 18

3.1.8 Reynolds Number…….. 19

3.2 Overview of Particle Treatment…… 19

3.2.1 Sphericity Definition…… 19

3.2.2 Sphericity Analysis and Average Value…… 20

3.2.3 Particle Average Diameter Value…….. 22

3.2.4 Particle Average Density Value…… 23

3.3 Overview of Saltation Mechanics…… 23

3.3.3 Modes of Transport…… 24

3.3.4 Lift versus Splash…… 25

4 Overview of CFD Principles…… 26

4.1 Gambit Modeling…… 26

4.1.1 Overview…… 26

4.1.2 Trips…… 27

4.1.3 Meshing and Y+…… 29
4.2 FLUENT Modeling…… 30
4.2.1 Overview…… 30
4.2.2 Coupling Effects…… 31
4.2.3 Residuals…… 31
4.2.4 Limitations…… 31
4.2.4.1 Particles as Streams…… 31
4.2.4.2 Particle Injections…… 32
4.2.4.3 Particle Bounce…… 32
4.3 Approximation and Implementation of Fluid Mechanics Principles…… 33
4.3.1 FLUENT Treatment of Navier-Stokes Equations……. 33
4.3.2 FLUENT Treatment of Nonspherical Particle Drag……... 34

5 Methods and Procedures…… 36
5.1 Analytical…… 36
5.1.1 Knudsen Number……. 36
5.1.2 Reynolds Number…… 36
5.1.2.1 MARSWIT Tunnel…… 36
5.1.2.2 MARSWIT Particle…… 37
5.1.2.3 Titan Particle……. 38
5.1.3 Hydraulic Diameter and Turbulence Approximation….. 38
5.1.4 ImageJ Particle Tracking…….. 38
5.1.4.1 Noise and Particle Resolution……. 38
5.1.4.2 Trajectory Curves…… 39
5.1.5 Calculating Robins-Magnus Force Effect Correction….. 39
5.2 Computational…… 41
5.2.1 Setting Initial Conditions……. 41
5.2.1.1 Matching Test Section Velocity…… 41
5.2.1.2 Determining Velocity Components…… 42
5.2.2 Operating Conditions…… 47
5.2.2.1 Earth…… 47
5.2.2.2 Titan…… 47
5.2.3 Applying Body Force Terms as Acceleration Corrections 48

6 Results, Validation, and Projections…….. 49
6.1 MARSWIT Tunnel Results and Comparison to FLUENT……. 49
6.2 Initial MARSWIT Results for Four Cases…… 51
6.3 MARSWIT Results with Magnus Effect with Uncertainty Bounds
…… 55

6.4 Titan Projections for Specific Conditions…….. 58
6.5 Predicted Constant Spin Rates Required versus Relative Velocity…… 64
6.6 Predicted Static Threshold Friction Speed for Titan …….. 65

7 Uncertainty and Error Estimates……. 69
7.1 Overview…… 69
7.2 Selection Bias……. 69
7.3 Stochastic Effects…… 70
7.4 Small Particle Cohesive and Electrostatic Effects……. 70
7.5 Spin Rate Value and Non-constant Spin Rate Effect……. 71
7.6 Density, Size, and Mass…….. 71
7.7 Noise in Data……. 72
7.8 Summary……. 72

8 Summary and Future Work……. 73
8.1 Summary and Review of Thesis…… 73
8.2 Future Work…… 74

List of References…… 76

Vita

List of Tables

3.1 Platonic Solid Method (PSM) Sphericity Values. [36]…… 21

3.2 Walnut Shell Density Results with Variation, High, and Low Values…… 23

3.3 Particle Size Characterization by Diameter (m)…… 24

6.1 Saltation Height to Length Ratios……. 63

7.1 High and Low Variation for Walnut Shell Density Determination…….. 71

List of Figures

1.1 Titan aeolian dune formations (courtesy of JPL)…… 1

2.1 MARSWIT Surface Wind Tunnel at NASA Ames (courtesy of NASA)…….. 7

3.1 Particle Downstream-velocity versus Time in MARSWIT Tunnel…… 12

3.2 Magnus Force Depiction as Cross-Product Result of $\overline{Q}_p$ and $\overline{v}_R$…… 12

3.3 $C_{L\Omega}^{*}$ versus Ω_{p}^{*}, based on Reynolds Number…… 14

3.4 Comparison of (non-dimensional) velocity profiles in turbulent (left) and laminar (right) boundary layers…… 16

3.5 Model Interior View of the MARSWIT Wind Tunnel, showing Boundary Layers and the "No-Slip" Condition…… 16

3.6 Microscopic Analysis of MARSWIT Particle. [36]……. 20

3.7 Ellipsoid Axis Convention. [36]…… 21

4.1 Selection of 3D Local Element as used in FLUENT. [7]……. 27

4.2 Boundary Layer Trip Device in MARSWIT Tunnel…… 28

4.3 Typical Linear-log Profile Showing Transition from Laminar to Turbulent Flow. [34]……. 30

4.4 Coefficient of Restitution Definition. [34]…… 33

5.1 Tracking of Walnut Shell Particle in Fully Turbulent Flow at 5.45 m/s…… 39

5.2 Particle x-direction Component Position versus Time Curve and Velocity Time Derivative Run 21S…… 43

5.3 Particle y-direction Component Position versus Time Curve and Velocity Time Derivative Run 21S…… 43

5.4 Particle x-direction Component Position versus Time Curve and Velocity Time Derivative Run 21M…… 44

5.5 Particle y-direction Component Position versus Time Curve and Velocity Time Derivative Run 21M……. 44

5.6 Particle x-direction Component Position versus Time Curve and Velocity Time Derivative Run 23!C…… 45

5.7 Particle y-direction Component Position versus Time Curve and Velocity Time Derivative Run 23!C…… 45

5.8 Particle x-direction Component Position versus Time Curve and Velocity Time Derivative Run 23C…… 46

5.9 Particle y-direction Component Position versus Time Curve and Velocity Time Derivative Run 23C……. 46

6.1 Test Section Tripped Velocity for Empirical vs. FLUENT…… 50

6.2 Simulated trajectories for both spherical and non-spherical particles at ρ=1066 kg/m^3…… 51

6.3 Trajectory Plots for Phi = 1.0 and 0.4 without (top) and with (bottom) Magnus Effect Run 21S…… 52

6.4 Trajectory Plots for Phi = 1.0 and 0.4 without (top) and with (bottom) Magnus Effect Run 21M…… 53

6.5 Trajectory Plots for Phi = 1.0 and 0.4 without (top) and with (bottom) Magnus Effect Run 21!C…… 54

6.6 Trajectory Plots for Phi = 1.0 and 0.4 without (top) and with (bottom) Magnus Effect Run 21C…… 55

6.7 Trajectory Plots for Phi = 1.0 and 0.4 with Magnus Effect and Error Bounds Run 21S…… 56

6.8 Trajectory Plots for Phi = 1.0 and 0.4 with Magnus Effect and Error Bounds Run 21M…….. 57

6.9 Trajectory Plots for Phi = 1.0 and 0.4 with Magnus Effect and Error Bounds Run 23!C……. 57

6.10 Trajectory Plots for Phi = 1.0 and 0.4 with Magnus Effect and Error Bounds Run 23C…… 58

6.11 Titan Average Particle (TAP) Position versus Speed…….. 59

6.12 Titan Particle Size Variation versus TAP Position Plots, 1.35 m/s..…… 59

6.13 Titan Particle Size Variation versus TAP Position Plots, 2.08 m/s..…… 60

6.14 Titan Particle Size Variation versus TAP Position Plots, 2.98 m/s…….. 60

6.15 Titan Particle Density Variation versus TAP Position Plots, 1.35 m/s……. 61

6.16 Titan Particle Density Variation versus TAP Position Plots, 2.08 m/s……. 61

6.17 Titan Particle Density Variation versus TAP Position Plots, 2.98 m/s……. 61

6.18 Titan Particle Phi (ϕ) Variation versus TAP Position Plots, 1.35 m/s…….. 62

6.19 Titan Particle Phi (ϕ) Variation versus TAP Position Plots, 2.08 m/s…….. 62

6.20 Titan Particle Phi (ϕ) Variation versus TAP Position Plots, 2.98 m/s…….. 63

6.21 Apparent Earth Gravitational Force due to Magnus Force and Differential Velocity…….. 64

6.22 Apparent Titan Gravitational Force due to Magnus Force and Differential Velocity…….. 65

6.23 Threshold Friction Speed versus Particle Diameter for Different Planetary Bodies. [12]…… 66

6.24 Particle Fluid Threshold Speed versus Size for Earth and Titan……. 67

6.25 Comparison for Identical Earth and Titan Particles at Equivalent Initial Forces.. 67

Nomenclature

Symbols Used

a	acceleration
A, D	characteristic reference area
a, b, c	ellipsoid length values
C_d	drag coefficient
$C^*_{L\Omega}$	spin lift force coefficient
C_μ	viscosity coefficient
C_p	pressure coefficient
C_s	roughness constant
d	molecular diameter
D_F	drag force
D_H	hydraulic diameter
D_p	particle diameter
F	force
F_{mag}	Magnus force
g	gravity
I	turbulent intensity
k	turbulent kinetic energy transport coefficient
K_s	roughness height
K_S^+	dimensionless roughness height
Kn	Knudsen number

L	length
ℓ	turbulence length scale
m	mass
N_A	Avogadro's number
R	specific gas constant in air
r	radius of particle
Re	Reynolds number
Re_p	particle Reynolds number
Re_{SPH}	sphere Reynolds number
s	surface area of sphere
S	surface area of irregular particle
t	time
T	absolute temperature
T_o	standard temperature
u, v, and w	fluid velocity components
u_{avg}	x velocity, time-averaged
$\bar{u}[t]$	wind velocity
u_{*_t}	static threshold friction speed
u^+	non-dimensional velocity
$\overline{u_x}$	mean x-direction velocity
$u_x{}'$	fluctuating x-direction velocity
V	component velocity vector
V_1	Earth wind velocity
V_2	Titan wind velocity

$\bar{v}[t]$	particle velocity
$\bar{v}_R$	relative wind velocity
W	width
y^+	non-dimensional wall distance
Z	Bagnold's factor
λ	bulk viscosity
μ	dynamic viscosity
ρ, ρ_a	atmospheric density
$\bar{\Omega}_p$	nominal particle angular spin velocity
τ_{xy}	shear of x in y direction
λ^*	characteristic length scale
ε	turbulence dissipation rate transport coefficient
υ	kinematic viscosity
μ	dynamic viscosity
ϕ	sphericity shape factor
ρ_p	particle density
Ω_e	CFD element
δ_{ij}	Kronecker delta
μ_o	viscosity at standard temperature

Chapter 1

Introduction

Equipped with his five senses, man explores the universe around him and calls the adventure Science.

– Edwin Powell Hubble [*The Nature of Science*, 1954]

1.1 Overview and Purpose of this Thesis

Wind driven particulates have been recognized for decades as a major determinant of geomorphology, not only on Earth, but also on other bodies in the Solar System including Mars, Titan, and Venus. Moreover, recent imaging by the Cassini spacecraft has unexpectedly revealed that aeolian dunes cover about twenty percent of Titan's surface [19, 24]. Therefore, an understanding of wind driven sediment transport is key to explaining much of Titan's surface.

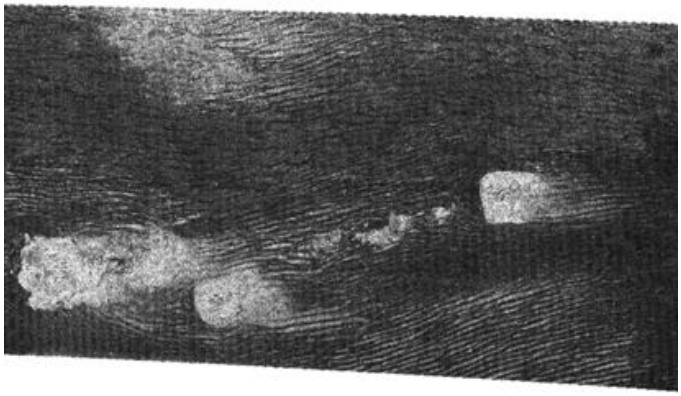

Figure 1.1: Titan aeolian dune formations (courtesy of JPL)

Substantial efforts have been made over the last few decades to understand aeolian processes using specialized wind tunnels, field studies, and, more recently, numerical simulations [17, 3, 4]. In this thesis, this author has presented:

1) a model of aeolian sediment transport using a commercially available computational fluid dynamics (CFD) software package manufactured by Ansys, Inc., called FLUENT.
2) comparison of numerical results with experimental data obtained in wind tunnel testing currently in progress at the NASA Ames Research Center Planetary Aeolian Laboratory (PAL).
3) comparison of parametric variation for a set of specific initial conditions on Titan.
4) direct comparison of Earth and Titan trajectories for equivalent initial forces.

The experimental data from NASA Ames PAL were used to validate the numerical model developed. This thesis's ultimate completed objective was to develop an experimentally validated computational approach for modeling aeolian sediment transport on Titan. Once a reliable numerical model was available, it enabled relatively rapid and low-cost simulations of aeolian processes over a wide range of particle sizes and environmental conditions.

In the study, sieved walnut shell particles with diameters of 175-250 microns were placed on the test section floor, the tunnel was started, and the free stream airspeed was raised to between ~2.5 and 7.5 m/s, depending on the case. A Phantom v12 high-speed camera was used to image the resulting particle motion at 1000±1 frames per second, and the open source software, ImageJ [1], was used to evaluate particle motion.

The model was finally used to calculate mean saltation trajectories and saltation height to saltation length ratios on Titan for a specific initial condition set for surface airspeeds, grain densities, grain shapes, and grain sizes. It is hoped this model will reduce the need for as many expensive and time-consuming wind tunnel tests, and will increase the range of potential operating conditions that can be evaluated. With relatively minor modifications, the same methodology can be used on other planetary bodies, with vastly different atmospheric or particle characteristics.

1.2 History and Current State of Aeolian Transport

Modern, particle saltation theory was begun in large part by British Army Officer and scientist Brig. Ralph A. Bagnold, who published a particle-approach to sand research in his seminal and oft-cited 1941 book, The Physics of Blown Sand and Desert Dunes. Throughout the early 1940's and until the 1960's, his theories and empirical methods in [6], and other results largely published at the Royal Society Proceedings in London, represented the bulk of Earth saltation studies until expansive efforts in the 70's, and 80's by researchers such as White, Greely, and Iverson (among others) who completed analogue experimentation for off-earth environments of Venus, Mars, and (now) Titan. Papers showing the history of the evolution of particle saltation and static threshold friction speed investigations are notably [12, 13, 14, 16] and [29, 30, 31].

Greely, Iverson, and White carried out experiments to determine critical parameters for the Viking landers and other robotic missions with respect to particle flux, sediment transport characteristics, suspension, and threshold friction speed ranges the landers would experience. These data were obtained in the Venus Wind Tunnel (VWT) and the Mars Atmospheric Surface Wind Tunnel (MARSWIT), both at NASA Ames, which were capable of simulating important aerodynamic properties, such as atmospheric pressure, turbulence, and boundary layer (BL) thickness, discussed more in Chapter 3.

The current state of particle surface dynamics is robust, and renewed interest from scientists at the intersection of physics, aerodynamics, and geology have created a multidisciplinary framework in which future experiments can be accomplished with enhanced interdisciplinary insight. Numerical studies from Kok [17] with COMSALT, a MATLAB based saltation solver package, and other studies by Almeida et al. in 2006 and 2008 [3, 4] using FLUENT have shed varying degrees of insight, and help translate an accurate model from a realm of physical interaction and chaos, to one of accurate digital interactions and repeatability.

1.3 The Case for CFD Modeling of Aeolian Transport

It is generally acknowledged that the modern world is increasingly relying on computers to do the mundane, repetitive tasks that in years past have been entirely done by hand, but while

wondrous and productive, care must be taken to not utilize the abilities computers present us as "black boxes." With that said, CFD approaches using MATLAB or FLUENT serve a vital role in reducing the number of hours an operational wind tunnel needs to be utilized and maintained or upgraded for new projects.

For example, the previous Venus Wind Tunnel is being modernized and re-instrumented to provide new data for Titan, to become the new Titan Wind Tunnel (TWT). While it is certainly essential to have a "real world" data generator, there is a large window in which CFD can be used to generate initial data for given conditions, making the down-time experienced by the installation less critical. Furthermore, if data for various locations need to be collected, CFD can be instantly configured to the new demands placed on it, while an entirely new tunnel would have to be approved, financed, and built. While the TWT was being constructed, the MARSWIT tunnel was run at ambient pressures to prove techniques, to generate saltation data, and to provide raw data, verifying the application of FLUENT in this thesis.

Lastly, it would take several thousand dollars per hour of run-time for a typical wind tunnel to generate useful data. While, CFD licenses can be a few to several thousands of dollars, once the first cost has been paid, CFD results can be generated for the distributed cost that a server farm will impose on an organization, since other agencies in that organization can use CFD for their purposes as well. As a result, marginal costs after the license is paid are minimal to run CFD cases, even when such runs take weeks or months to complete. For our purposes, the runs completed for this thesis averaged on the order of hours to days to converge, so the cost-benefit of using CFD versus wind tunnels (when data can be verified as accurate) is greatly increased. Of critical importance, some parameters (like gravity) will never be simulated on Earth, but can be simulated relatively easily in CFD.

However, before any reliance can be placed on the results of a CFD simulation, the model must be validated against experimental data. As a result, wind tunnel experimentation and CFD are often used together, with the tunnel providing a data set against which the numerical modeling is tested; often this results in improvements and modifications of the numerical model to bring its results into better agreement with experimental observations.

Ansys FLUENT is among the best known of the commercial CFD packages, and it has been applied and validated over an enormous range of applications [8, 23]. Lagrangian particle

trajectory calculations are within the scope of FLUENT's computational envelope. In the current work, FLUENT is used to model aeolian sediment transport and will compare the numerical results to experimental data. Modifications will be made to the numerical model until it is able to match experimental observations, and then the model will be applied to Titan surface conditions that cannot be easily and reliably replicated on Earth.

1.4 Section Summary

The overall rationale for this thesis was to provide a model that can be followed to generate saltation data when known wind tunnel results exist for comparison, and to generate saltation data under very specific initial conditions on Titan. Future work may involve applying the FLUENT model given initial saltation from static threshold conditions as this was not possible due to time constraints and modeling challenges. Setting initial velocity vectors in the CFD model, which were deduced from empirical trajectories captured by video particle tracking software, an excellent correlation for known trajectories was obtained (within uncertainty bounds, and when using parameters which were observed from particles used in the original NASA Ames experiments). Similar techniques were then applied through FLUENT to produce a parametric study of saltation trajectory pathlengths by varying size, density, and particle sphericity (particle shape parameter).

Finally, because pressure differentials produce the change in force which lead directly to initial velocities, a dynamic pressure formula was used to estimate what corresponding Titan velocity would be needed to match the velocity vectors generated on Earth (assuming all other parameters equal); in this way, this thesis can present the final parametric study, and then present a brief, direct comparison of estimated trajectories for the same initial conditions, without having static threshold friction data available. The main focus for this work will be comparison of CFD to MARSWIT results, and the generation of Titan results for specific initial conditions.

Chapter 2

Background

Science, in the very act of solving problems, creates more of them.

– Abraham Flexner [*Universities*, 1930]

2.1 Summer Research at NASA Ames

This thesis was only possible after first having learned how to operate the gridding program, GAMBIT, part of the initial modeling package grouped within Ansys FLUENT, and also learning how to operate FLUENT. After intensive months of tutorials, and intimate reading of FLUENT User Documentation, initial results were generated and presented to the Titan Research Team.

In the summer of 2010, between June and July, this author and Dr. J. Evans Lyne were invited to NASA Ames Moffett Field to assist directly with the research effort at the MARSWIT tunnel, which led to the data logging of more than 14GB of trajectories on high-speed digital film. The CFD effort began with verifying that the fluid inside the tunnel behaved as a continuum with respect to the particles by calculating the Knudsen number for the tunnel (details in Chapter 3). Once at NASA Ames, the author was able to generate an accurate 3D flow-field for the continuum inside the tunnel for the fully developed, turbulent flow that was verified by Reynolds number calculation, with details also in Chapter 3.

Using the results generated up until the summer session, it was possible to achieve reasonable agreement for CFD versus empirical data to within 10-15% of normalized downstream velocity as a function of height, with boundary layer trip devices modeled. The next objective would be to incorporate particles into the continuum and generate trajectory data for the two-phase flow that resulted.

Shortly after the summer and back at The University of Tennessee, the author successfully achieved the trajectory goal for CFD walnut shell particles with diameters of 175-250 microns, with an unknown size distribution, although bell distribution is assumed. Despite best efforts to modify the GAMBIT gridding model, which was then imported into FLUENT with different approaches, static threshold friction speed data was not able to be replicated, but trajectory data was promising. Therefore, despite that challenge, since known sizes of particles were placed on the test section floor of MARSWIT at approximately six meters from the inlet end of the tunnel, it was decided to concentrate on modeling the trajectories for the initial conditions observed from the high-speed video. Using the calculated initial velocities and vectors for each specific "best-observable" case we selected from the larger group, the four representative runs in this thesis were intensively studied with the intention of applying the methodology to a specific initial condition case-set for Titan.

2.2 MARSWIT Wind Tunnel Specifications at NASA Ames

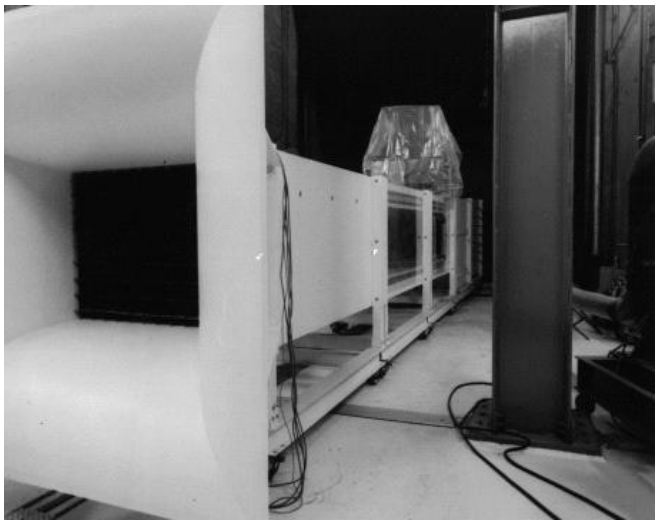

Figure 2.1: MARSWIT Surface Wind Tunnel at NASA Ames (courtesy of NASA)

The MARSWIT tunnel used for this work was specifically designed for atmospheric boundary layer studies. It is a variable-speed, continuous, open circuit tunnel with a test section 1.0 m by 1.2 m in size; the facility is able to operate at pressures from 5.5 millibar to one bar. Boundary layer trips near the tunnel inlet insure a fully developed, turbulent boundary layer in the test section. Wind speed and centerline velocity profiles can be measured with a traversing pitot tube, and the geometry of the tunnel to be modeled from direct measurements in GAMBIT is 0.9966 m in height by 1.218 m in width and approximately 12.19 m in total length from the inlet bell-end. The GAMBIT test section was nominally spaced between 6.0 m to ~6.5 m as measured from the observation window. Location of the free-stream traversing pitot tube was 6.445 m from the inlet and 0.00635 m from center. Traverse position data measurements ranged from the floor at 0.0 m to 0.363 m toward the ceiling. Wind velocities can be varied from 0 to 12 m/s at 1 bar and up to 150 m/s at 5 mb pressure.

2.3 American Geophysical Union (AGU) Fall Meeting

During the winter of 2010, The Titan Research Team met in San Francisco at the American Geophysics Union annual conference, where the author presented an abstract on current results on trajectories for MARSWIT. The trajectories found in Figure 6.2 show ideal particle tracks for smooth spheres as well as trajectories for differing values of sphericity (value characterizing “roundness” of a particle). A detailed explanation is found in Chapter 3, but briefly, sphericity is the ratio of particle’s surface area divided into the surface area for a perfect sphere of the same volume (value is always < 1).

Chapter 3

Overview of Theoretical Principles and Mechanics

I have had my results for a long time, but I do not yet know how I am to arrive at them.

– Karl Friedrich Gauss

3.1 Overview of Fluid Mechanics Principles

Since the core physics of particle-atmosphere interaction lies in the realm of fluid mechanics, it seemed reasonable to begin with a brief overview of the principal governing equations for that field. The principal elements for use and understanding of FLUENT's results are the pivotal non-linear set of equations generally known as the Navier-Stokes equations (after Frenchman M. Navier and Englishman G. Stokes) [5], Robins-Magnus force effect (named for B. Robins and H. Magnus), drag on a body, Knudsen number (after D. Knudsen [33]), hydraulic diameter, turbulence length scales and model, and a discussion on Reynolds number (which was discovered by G. Stokes, and popularized by O. Reynolds) [5].

3.1.1 Navier-Stokes Equations

Basic fluid dynamics begins with 4 foundational principles:

1) Conservation of Mass (Continuity)
2) Newton's Second Law of Motion (Momentum Conservation)
3) The First Law of Thermodynamics (Energy Conservation)
4) The Second Law of Thermodynamics (Irreversible Processes)

The first two principles are needed to derive the equations applicable to MARSWIT tunnel flows. If one begins with the viscous force equations that result from application of Newton's Second Law:

$$\boldsymbol{F} = m * a \qquad (3.1)$$

F = force, m = mass, and a = acceleration, then one can derive the conservative or non-conservative form of the momentum transfer equations for u, v, and w velocity directions for incompressible flow as:

$$\rho\frac{\partial u}{\partial t} + \rho u\frac{\partial u}{\partial x} + \rho v\frac{\partial u}{\partial y} + \rho w\frac{\partial u}{\partial z} = -\frac{\partial p}{\partial x} + \frac{\partial}{\partial x}\left(\lambda\nabla\cdot\boldsymbol{V} + 2\mu\frac{\partial u}{\partial x}\right) + \frac{\partial}{\partial y}\left[\mu\left(\frac{\partial v}{\partial x} + \frac{\partial u}{\partial y}\right)\right] + \frac{\partial}{\partial z}\left[\mu\left(\frac{\partial u}{\partial z} + \right.\right.$$

$$\partial w \partial x \qquad (3.2)$$

$$\rho\frac{\partial v}{\partial t} + \rho u\frac{\partial v}{\partial x} + \rho v\frac{\partial v}{\partial y} + \rho w\frac{\partial v}{\partial z} = -\frac{\partial p}{\partial y} + \frac{\partial}{\partial x}\left[\mu\left(\frac{\partial v}{\partial x} + \frac{\partial u}{\partial y}\right)\right] + \frac{\partial}{\partial y}\left(\lambda\nabla\cdot\boldsymbol{V} + 2\mu\frac{\partial v}{\partial y}\right) + \frac{\partial}{\partial z}\left[\mu\left(\frac{\partial w}{\partial y} + \right.\right.$$

$$\partial v \partial z \qquad (3.3)$$

$$\rho\frac{\partial w}{\partial t} + \rho u\frac{\partial w}{\partial x} + \rho v\frac{\partial w}{\partial y} + \rho w\frac{\partial w}{\partial z} = -\frac{\partial p}{\partial z} + \frac{\partial}{\partial x}\left[\mu\left(\frac{\partial u}{\partial z} + \frac{\partial w}{\partial x}\right)\right] + \frac{\partial}{\partial y}\left[\mu\left(\frac{\partial w}{\partial y} + \frac{\partial v}{\partial z}\right)\right] + \frac{\partial}{\partial z}\left(\lambda\nabla\cdot\boldsymbol{V} + \right.$$

$$2\mu\partial w\partial z \qquad (3.4)$$

where λ is the bulk viscosity, μ is the dynamic viscosity, **V** is the component velocity vector, and ρ is the density. For our purposes, FLUENT is solving for an incompressible flow. If one starts with the principle that mass is neither created nor destroyed, then for a flow field [5]: mass in = mass out, and net mass flow out of the control volume through surface **S** = time rate of decrease of mass inside control volume **V**, where normal (n) in-flow or out-flow, depending on sign is:

$$\rho * V_n * dS = \rho * \boldsymbol{V} \cdot \boldsymbol{dS} \quad (3.5)$$

Then the continuity equation can be expressed as:

$$\frac{\partial \rho}{\partial t} + \nabla \cdot (\rho \boldsymbol{V}) = 0 \qquad (3.6)$$

Combining the Navier-Stokes equations with equation 3.6 above (the continuity equation reduced, from volume integral-form, to partial differential form at a point), then for a control volume, with known boundary conditions, a solution can be approximated [5]. Essentially, this is what FLUENT does for each control volume it generates from GAMBIT, and passes along to the subsequent control volume in line. The error remaining after each iteration, the "residual," is steadily reduced until the solution converges below a set residual value.

3.1.2 Robins-Magnus Force Effect

Robins-Magnus effect is the effect seen as an increased curvature of a body's flight through a fluid as a result of spin. The methodology for determining Robins-Magnus force on spinning particles involves a cross product of the angular spin velocity of the object and the relative velocity vector of the fluid elements surrounding it.

From [21] and [17], the first step was to determine the relative velocity difference between the particle and the air flowing past it as it saltates and spins. To approximate the speed of the particle throughout the entire flight down the wind tunnel, on all cases this author plotted particle x-velocity (down the tunnel) and took the average of the maximum and minimum values from FLUENT results.

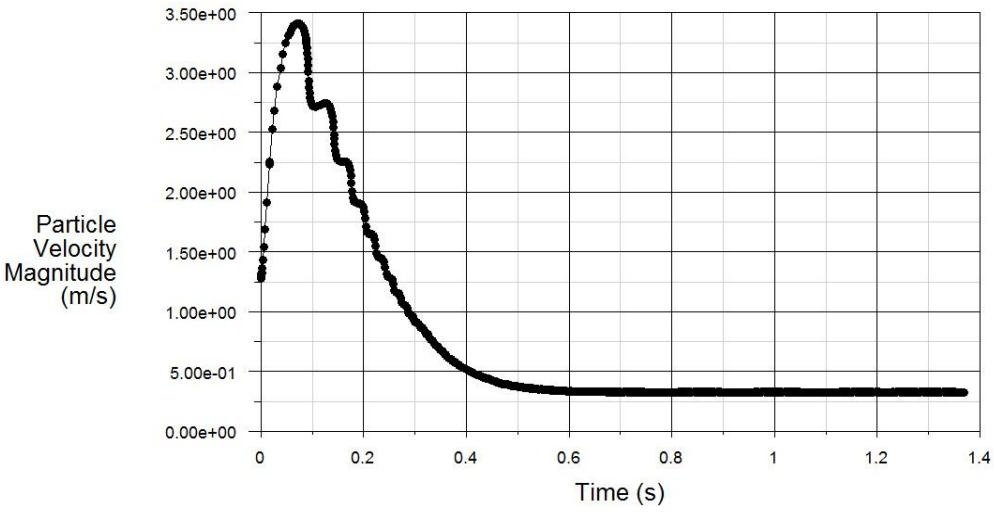

Figure 3.1: Particle Downstream-velocity versus Time in MARSWIT Tunnel

An overview of the relative velocity calculation is demonstrated visually by Figure 3.2 below:

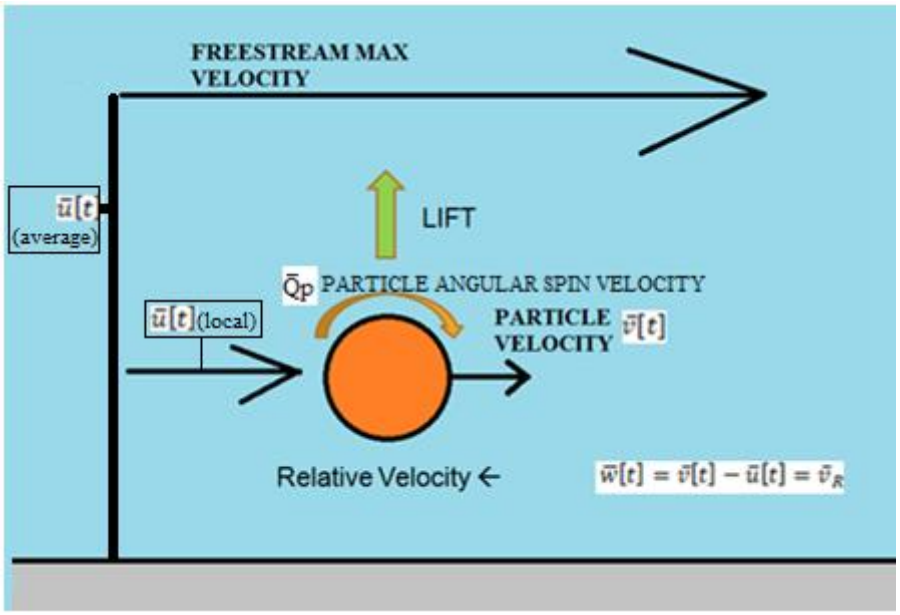

Figure 3.2: Magnus Force Depiction as Cross-Product Result of $\overline{Q}_p$ and $\overline{v}_R$.

This value is particle velocity in subsequent equations: ($\bar{v}[t]$). The average wind velocity is $\bar{u}[t]$ (average) and was determined from an average value of maximum and steady-state tunnel speeds. Local wind velocity is $\bar{u}[t]$ (local) and was determined from an average value of

velocity near the particle. Taking the time component out by time-averaging (which reduced the unsteady effects of turbulence at small time scales):

$$\bar{v}[t] - \bar{u}[t] = \bar{v}_R \qquad (3.7)$$

Where [16] gives:

$$F_{mag} = \frac{\pi}{8} * \rho_a * D_p^3 * C_{L\Omega}^* * [\bar{\Omega}_\mathrm{p} \times \bar{v}_R] \qquad (3.8)$$

For each case, F_{mag} is Magnus force, ρ_a is atmospheric density, D_p is particle diameter, $C_{L\Omega}^*$ is the spin lift force coefficient, $\bar{\Omega}_\mathrm{p}$ is the particle nominal angular spin velocity, and $\bar{v}_R$ was previously defined. Next, the process of determining the spin lift force coefficient involves determining the non-dimensional particle angular spin velocity Ω_p^* which is:

$$\Omega_\mathrm{p}^* = \frac{\bar{\Omega}_\mathrm{p} * D_p}{|\bar{v}_R|} \qquad (3.9)$$

After this value is determined for each particle diameter and relative local velocity, it is used in the graph below copied from [21], with the estimate for Reynolds number, which will be calculated in Chapter 5:

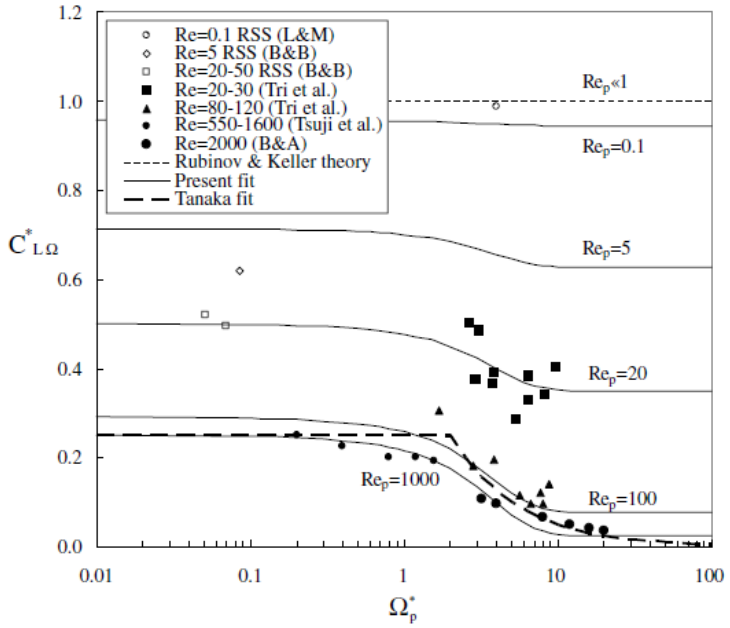

Figure 3.3: $C^*_{L\Omega}$ versus Ω^*_p, based on Reynolds Number.

Since the range of particle sizes and density is known, one can now solve for particle average mass. Once the force component is known for a constant spin rate, then the corresponding acceleration can be computed for a given particle mass, using Equation 3.1.

3.1.3 Particle Drag

In addition to accurately modeling the fluid flow field, reliable predictions of particle trajectories will require correct models of the interaction of the particles with the gas. Forces on the particles due to interaction with the atmosphere include aerodynamic drag, buoyancy, lift from pressure gradients (especially in the near wall regions where velocity and pressure gradients are the highest), and Magnus forces resulting from particle spin. The effect of particle entrainment on the flow field was not measured, although the effect may be small due to the relatively small number of particles entrained and the relatively large CFD tunnel area. For regular elements or (in this case), spherical particles, aerodynamic drag is typically given by:

$$D_F = \tfrac{1}{2}\,\rho\, V^2 C_d A \quad (3.10)$$

where D_F is the drag force, C_d is the coefficient of drag, ρ is the density, and A is a characteristic reference area of the object (typically a projected frontal area or cross-sectional area) [33].

3.1.4 Boundary Layer and Velocity Profile

Calculated particle trajectories will be determined largely by the assumed velocity profile of the fluid, so any attempt to predict accurate trajectories must begin with a reliable model of the fluid's motion. Therefore, before trying to model particle saltation, it is necessary to produce a validated flow field solution without any particles present. In fluid mechanics, the no-slip condition states that, for viscous flow, the fluid will have zero velocity relative to any solid boundary. This is caused by molecular viscosity at the atomic level and roughness height, which stops individual molecules at the surface, and pulls the air across the boundary thickness in layers as height is increased. It is governed by the shear stress formula:

$$\tau_{xy} = \mu * \frac{\partial u}{\partial y} \quad (3.11)$$

where τ_{xy} is shear stress of x in the y direction, μ is the dynamic (or molecular) viscosity, and $\frac{\partial u}{\partial y}$ is defined as the directional derivative of the downstream u-direction flow in the "up" or y-direction.

The velocity profile as a function of distance from away from the boundary (the tunnel floor in our case), depends critically on the state of the boundary layer, defined as the location in a flow where (from a boundary), the flow at any point reaches 99% of the value of the free stream airspeed [5]. The state of the boundary layer depends specifically on whether the layer is laminar or turbulent (smooth or chaotic, or predominantly viscous/molecular in its behavior). In general, the velocity profile above the wall is steeper for a turbulent than for a laminar boundary layer, as can be seen in Figure 3.4 below [5], due to the random nature of the velocity vectors, and the nature for the molecules of air to "carry" themselves further into the flow field) in such flows.

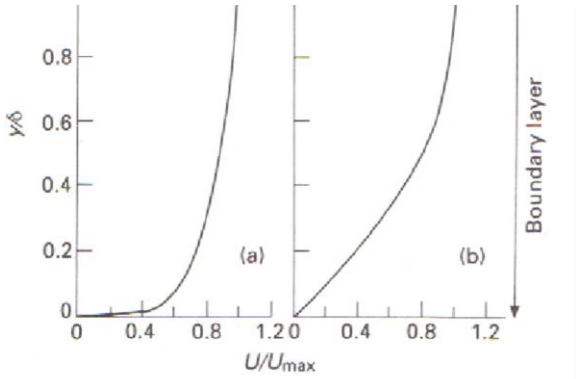

Figure 3.4: Comparison of (non-dimensional) velocity profiles in turbulent (left) and laminar (right) boundary layers.

Atmospheric boundary layers along planetary surfaces demonstrate similar characteristics, and are typically fully turbulent. Any effort to simulate atmospheric conditions and wind-borne sediment motion must assure a turbulent boundary layer.

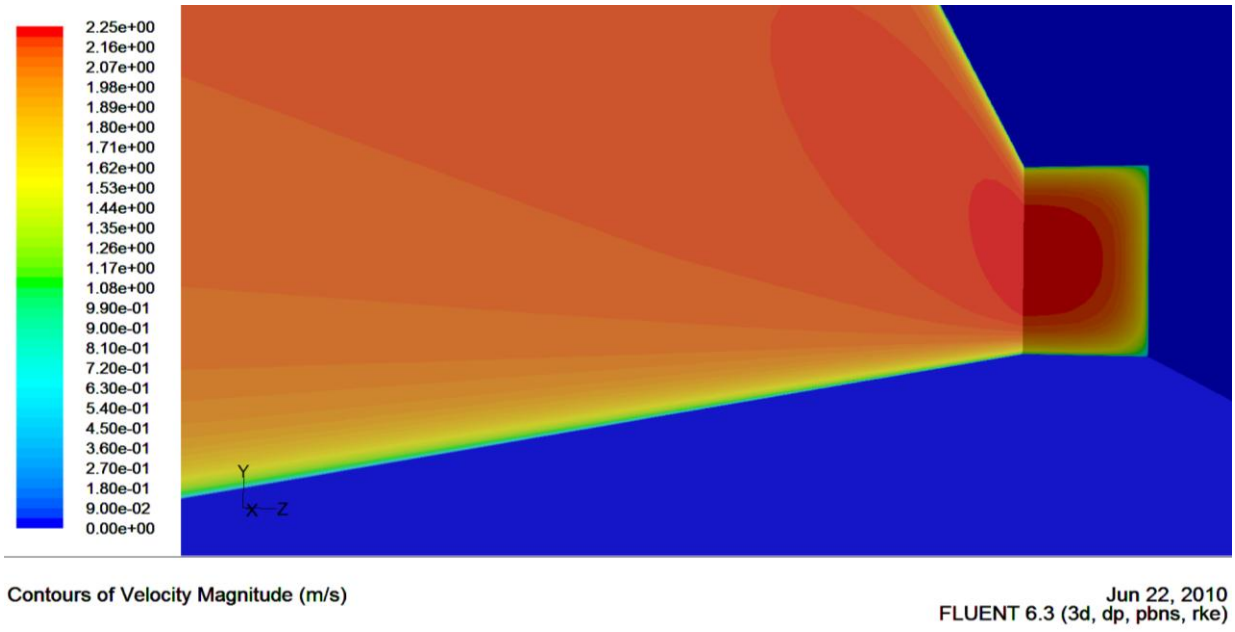

Figure 3.5: Model Interior View of the MARSWIT Wind Tunnel, showing Boundary Layers and the "No-Slip" Condition.

The boundary layer must be well defined and work in this area generally acknowledges a combination of layers present in the flow [5]. As an explanation for the normal-lift force responsible for oscillating and initiating saltation for particles at a given free-stream velocity and size, a thin, high-shear, turbulent boundary layer has been proposed, which allows high surface lift forces to develop. This work's focus has been on numerical technique on what will likely be the case in the environment, namely, a fully developed turbulent model, as used successfully by White [31] and others.

3.1.5 Knudsen Number

The Knudsen number is the ratio of the mean-free-path of a molecule (λ) to its characteristic dimension (D) and gives an indication of how to approach and solve the problem. If Kn is near or greater than one, meaning the mean-free path of the particle is on the order of the length scale of the environment, then statistical methods should be used and the flow cannot be considered a continuum.

- Kn < 0.001 Continuum
- 0.001 – 0.1 Slip Flow
- 0.1 – 10 Transition Flow
- > 10 Molecular Flow

The formula for Kn is [32]:

$$Kn = \frac{\lambda^*}{D} \qquad (3.12)$$

$$\lambda^* = \frac{RT}{\sqrt{2}\pi d^2 N_A P} \qquad (3.13)$$

In the mean-free-path formula, the specific gas constant for air is R, P is pressure, T is absolute temperature, N_A=6.0221E23 /mol (Avogadro's number), λ^* is the characteristic length scale, and d=4.00E-10 m, which is an approximate diameter for a typical gas molecule.

3.1.6 Hydraulic Diameter

As referenced in FLUENT documentation [34], turbulent intensity (I) inside the tunnel must be estimated and length scales (ℓ) govern the breakdown of the largest and smallest vortices of turbulence using the following formulas, based in part off hydraulic diameter of the tunnel (D_H, a measure to relate a non-circular cross-sectional area to that which would be similar to a circle for a given Re). For the purposes of CFD, the following equations were used to calculate I and ℓ [34]:

$$I = .16(Re_{D_H})^{-1/8} \qquad (3.14)$$

$$D_H = {2LW}/{L + W} \qquad (3.15)$$

$$\ell = 0.07(D_H) \qquad (3.16)$$

where L and W are length and width of the modeled tunnel, respectively in meters.

3.1.7 Turbulence Length Scales

FLUENT automatically computes the k-ε portion of the turbulent scheme in the CFD used in this thesis, where the values of turbulent intensity and the length scale are then used in the standard *k-ε* turbulent flow scheme of Launder and Spaulding [18]. Below, *k* in the first transport equation describes the turbulent kinetic energy creation, and *ε* in the second transport equation denotes the turbulent dissipation of the problem [9].

$$k = \frac{3}{2}(u_{avg}I)^2 \qquad (3.17)$$

$$\varepsilon = (C_\mu)^{\frac{3}{4}} * \frac{k^{\frac{3}{2}}}{\ell} \qquad (3.18)$$

The variables are as previously defined, constant Cμ=0.9 [33], and u_{avg} is the local x-velocity time-averaged value; buoyancy effects are ignored since heating terms are disregarded.

3.1.8 Reynolds Number

The Reynolds number at which a boundary layer transitions from laminar to turbulent is not a fixed value, but may vary from 2,300 to over 500,000, depending on the presence of disturbances to the flow, especially surface roughness [5]. Therefore, MARSWIT uses roughness elements on the tunnel floor, upstream of the test section to insure that the boundary layer is fully turbulent before it reaches the test section. The state of the boundary layer and the resulting velocity profile above the tunnel floor depend on the dimensionless Reynolds number, the ratio of inertial forces to viscous forces. The equation for Reynolds number (Re) is:

$$Re = \frac{\rho VD}{\mu} = \frac{VD}{\upsilon} \qquad (3.19)$$

where V is velocity of the flow, D is a characteristic length, υ is kinematic viscosity, ρ is the density, and μ is the dynamic viscosity.

3.2 Overview of Particle Treatment

3.2.1 Sphericity Definition

For particles whose shapes are non-spherical, a shape factor (ϕ) is used; this is given by:

$$\phi = \frac{s}{S} \qquad (3.20)$$

where "S" is the surface area of the irregular particle, and "s" is the surface area of a sphere of equal volume (this factor is always ≤1) [28]. The equation for the surface area and volume of a sphere is given as:

$$Surface\ Area\ (S.A) = 4 * \pi * r^2 \quad (3.21)$$

$$V = \frac{4}{3} * \pi * r^3 \qquad (3.22)$$

where r is defined as the radius of the particles in the study. FLUENT provides input parameters for analyzing particles with sphericity (Phi) value less than one in the Discrete Phase Model (DPM) it provides.

3.2.2 Sphericity Analysis and Average Value

John Hills, Titan research team member and recent graduate of The University of Tennessee, investigated obtaining ϕ using geometric analysis and microscopic evaluation. An average value for ϕ was determined to be approximately ~0.93 for sphericity from the ellipsoid method. This value was further confirmed through a geometric parametric study of non-spherical platonic solids as surrogates for walnut shell particles used in this study, as face number increased. Because of this research effort into defining a reasonable value for phi, the value of 0.93 was used in all FLUENT results presented, unless specifically mentioned. Below, a figure showing a typical walnut shell particle is presented from the microscopic analysis.

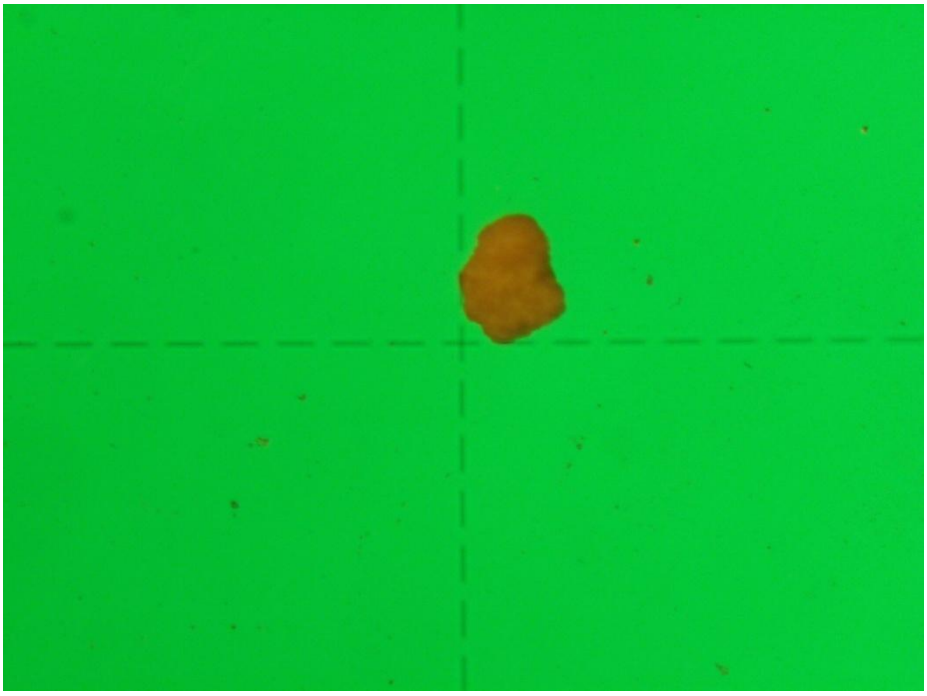

Figure 3.6: Microscopic Analysis of MARSWIT Particle. [36]

The approaches taken for determining appropriate values of Phi resulted in the Platonic Solid Model (PSM) and Ellipsoidal Model (EM).

1. *Platonic Solid Model*

This model involves using basic platonic solid shapes as estimates for actual particle volume and surface area. A table of each polyhedron and its associated ϕ value can be seen below:

Table 3.1: Platonic Solid Method (PSM) Sphericity Values. [36]

Picture of Platonic Solid	**Name of Platonic Solid**	**Sphericity (ϕ)**
	Tetrahedron (4 faces)	0.671139291
	Hexahedron (6 faces)	0.805995977
	Octahedron (8 faces)	0.845582521
	Dodecahedron (12 faces)	0.910453181
	Icosahedron (20 faces)	0.939325652

2. *Ellipsoidal Mode*

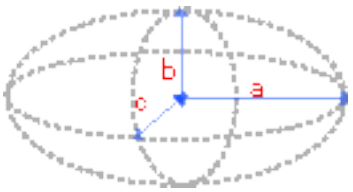

Figure 3.7: Ellipsoid Axis Convention. [36]

As the name suggests, an ellipsoid is used to approximate the volume and surface area of a particle. There are three dimensions to an ellipsoid (a, b, and c) in the scheme and rank magnitude is in agreement with "**a > b > c**" whenever possible. Of course, there is nothing preventing any combination of relation between a, b, and c. In fact, one can safely conclude that only the relative proportions between the three dimensions are important for calculating ϕ [36]. Relevant equations for combining the sphericity formula to allow for transformation of ellipsoid measurements to spherical equivalent values are:

$$V_{ellipsoid} = \frac{4}{3} * \pi * a * b * c \qquad (3.23)$$

$$Surface\ Area_{ellipsoid} = 4\pi(\frac{ab+ac+bc}{3})^{\frac{1}{p}} \qquad (3.24)$$

Where (a) is defined as the radius in microns along the x-axis, (b) is the radius along the y-axis, (c) is the radius along the z-axis, and $p \approx 1.6075$, yielding a relative error of at most 1.061% via Knud Thomsen's formula [36].

To get the new sphericity formula in terms of an ellipsoid, first let $V_{sphere} = V_{ellipsoid}$. From this equivalency, the relationship between r and a, b, and c is: $\boldsymbol{r = (a*b*c)^{1/3}}$. With this relationship, substitute into the SA_{sphere} equation, yielding $SA_{sphere} = 4*\pi*(a*b*c)^{2/3}$. Then, it is a matter of dividing, $\phi = SA_{sphere} / SA_{ellipsoid}$, which is only in terms of a, b, and c. These radii are determined from observation and measurement of particles as in Figure 3.6 [36].

3.2.3 Particle Average Diameter Value

Ro-Tap, Inc. manufactured the sieving machine which was used at NASA Ames during the summer of 2010 to isolate a small range of particle sizes to begin wind tunnel testing. Assuming a normal bell distribution in particle diameters from 175 to 250 microns, an average value of 213 microns was used in all runs requiring a mean value for size. A significant amount of error would be introduced if this assumption were incorrect.

3.2.4 Particle Average Density Value

Additionally, the published values for walnut shell density in open literature from manufacturers were found to be 1.2-1.4 specific gravity. This appeared to be somewhat higher than expected, so density experiments were conducted at the University of Tennessee to confirm values for density of walnut shell particles. Utilizing five different measurements, a known quantity of shell particles was placed in 25mL graduated cylinders with a previously recorded amount of 99% pure acetone (785 kg/m^3). From the displacement of the acetone, an average value of 1.0-1.1 specific gravity (1066 kg/m^3 is the value used in the CFD) was determined experimentally.

The mass balance had a nominal accuracy to within +/- 0.01 grams, but error analysis will be discussed in-depth in Chapter 7. Initial results for average density can be seen below in Table 3.2. The nominal value used for density of all particles from MARSWIT runs was 1066 kg/m^3, unless otherwise specified.

Table 3.2: Walnut Shell Density Results with Variation, High, and Low Values.

		Walnut Shell Density Results				
	Error (+/-)	Sample 1	Sample 2	Sample 3	Sample 4	Sample 5
Weight (g)	0.01	2.138	2.235	2.167	2.066	3.318
Volume (mL)	0.5	2.000	2.000	2.000	2.000	3.230
Density (kg/m^3)		1069	1118	1084	1033	1027
high variation (+)	*(kg/m^3)*	*363.0*	*378.7*	*367.3*	*351.0*	*192.0*
low variation (-)	*(kg/m^3)*	*217.8*	*228.0*	*221.2*	*210.6*	*140.1*
Average Density (kg/m^3)				**1066**		
high average value	*(kg/m^3)*			1397		
low average value	*(kg/m^3)*			862.7		

3.3 Overview of Saltation Mechanics

From the Encarta English Dictionary (North American Edition):

Saltation (noun) [sal·ta·tion] :

1. Jumping or jump – leaping or jumping, or a sudden jump or leap

2. Sudden change – development or transition that takes place in jumps or leaps

3. Abrupt evolutionary development – (Biology) the abrupt evolutionary development of a new species or property, especially as a result of genetic mutation

4. Jumping motion of particles – (Geology) the transportation of particles of soil or sand in the wind or in running water, characterized by bouncing movements.

3.3.1 Modes of Transport

Bagnold [6] was the first to propose the existence of the following modes of transport:

1) Creep: particles are pushed by direct pressure of wind on their surface. Large particles (usually >500 microns) cannot saltate due to their large comparative mass, and slide or roll across the surface in this movement mode [12].
2) Saltation: Fluid saltation [6], as opposed to "impact saltation," which will be discussed in the following section, is where wind shear across the top of a particle causes a lift force that then lofts the particle through the boundary layer, and into the free-stream airstream.
3) Suspension: for suspension, the particle fall velocity (μ_f) must be less than the wind friction velocity (μ_*) due to turbulence or eddies [2]). In essence, the local velocity fluctuations around a particle must be greater than the particle's terminal velocity.

Particles that undergo saltation can be characterized by size as Table 3.3 shows [14] below:

Table 3.3: Particle Size Characterization by Diameter (m).

Diameter sizes (m)	
Silt/Dust	.0000021- .00005
Fine sand	-.00002- 0.0002
Coarse sand	.00021- .002

It is chiefly the size, density, and shape of a particle which governs how and when it will move. The initial speed at which a particle at rest begins to move under the direct pressure and lift force combination from impacting wind is defined as the static threshold friction speed, shown below:

$$u_{*_t} = Zg(\rho_p - \rho_a)/\rho_a)^{1/2} \qquad (3.25)$$

where "g" is the local gravitational acceleration, D_p is the particle diameter, ρ_p is the particle density, and ρ_a is the gas-phase density. The constant Z=2.61 was determined experimentally from wind tunnel tests of sub-rounded quartz sand 100 microns in diameter [30]. The first sizes of particles to move are between ~70 and 500 microns and move in a series of hops [12].

3.3.2 Lift versus Splash

As mentioned, fluid saltation and impact saltation are two distinct forms of saltation. Once fluid saltation has been established, the steady-state for mode for saltation proceeds at a slightly lower free-stream velocity in typical cases because of the energy from the down-falling particles is transferred to the bed of grains, ejecting some particles into the free-stream.

Approximately 85% reduction in amount of energy needed to provide fluid saltation is needed in splash mechanics for a reptation effect, due to energy injected from the falling particle [16]. The overall effect is smaller particles most-of-all (< 62.5 microns), and all particles in general, begin saltation or suspension earlier because enough energy is obtained to break the small particle cohesive forces which would otherwise keep them attached to the ground and each other [12]. The model FLUENT used was not capable of reproducing this parameter for this thesis, although COMSALT [17] models now have the recent ability to model such effects.

Chapter 4

Overview of CFD Principles

The universe is full of magical things patiently waiting for our wits to grow sharper.

– Eden Phillpotts [*A Shadow Passes*]

4.1 Gambit Modeling

4.1.1 Overview

The first step in developing a CFD solution for any flow field is to generate an appropriate computational grid. At the nodes of this grid, the governing set of equations will be solved iteratively to converge on values of the important flow parameters such as flow velocity and direction, pressure, etc. Establishing the grid can be a substantial task, and this typically is accomplished with the use of a program designed specifically for this purpose. GAMBIT is the algorithm used in conjunction with FLUENT to model the physical environment and develop the grid.

CFD models can have hundreds of thousands to millions of nodes and require many hours for a single solution. Therefore, it is desirable to model the physical environment in the most efficient manner possible. For this thesis, since the MARSWIT facility had bi-lateral symmetry, the gridded model was simply reflected along the x-y plane to reduce the computational workload. The geometry of the tunnel as modeled is 0.9966 m in height by 1.218

m in width and approximately 12.19 m in total length from the inlet bell-end. The resulting computational grid representing the MARSWIT facility had approximately 671,000 nodes.

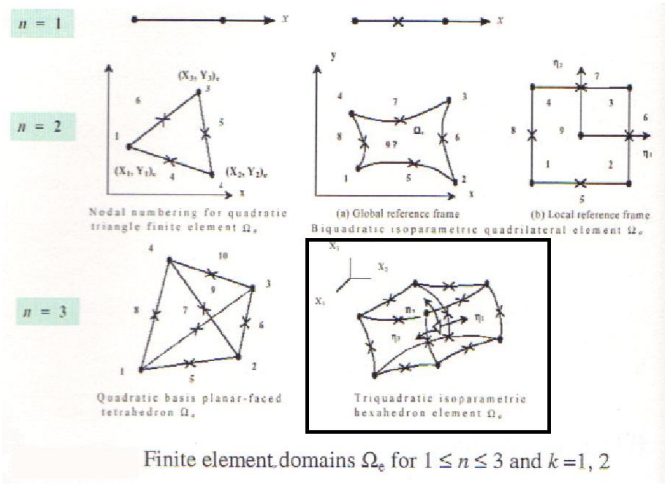

Figure 4.1: Selection of 3D Local Element as used in FLUENT. [7]

The FLUENT CFD finite element geometrical shape chosen was a hexahedron element, Ω_e, for an N=3 environment, as shown in Figure 4.1 above, because such a shape minimizes skewness of the control volumes. It is from the center-reference position of each of these nodes that FLUENT calculates and passes on flow-field properties and iterative solutions [34].

4.1.2 Trips

To ensure the BL is fully rough, fully turbulent flow, turbulent boundary layer trips were modeled in GAMBIT and passed to FLUENT. Surface properties for roughness height (K_s) and roughness constant (C_s) were determined through computation of a dimensionless roughness height parameter, K_S^+, setting the log-intercept for $\Delta B = 5.0$ (as seen in Figure 4.3), while using von Kármán's constant = 0.4187 [34][32].

Since naturally occurring turbulent flow over terrain is difficult to reproduce exactly in a boundary layer wind tunnel, turbulent trips had been added to MARSWIT. The MARSWIT flow trip devices can be seen in Figure 4.2 below which shows the trip boards with pebbles from the inlet at 0.0 m to 2.2098 m and 0.0756 m from the walls. The dimensions of measurement presented near the pebbles are in inches in Figure 4.2. The types of fluid flows which comprised

the majority of particle transport on any surface are almost always fully turbulent due to the continuous injection of external energy into the system, which is fundamental to sustaining and understanding the nature of these flows.

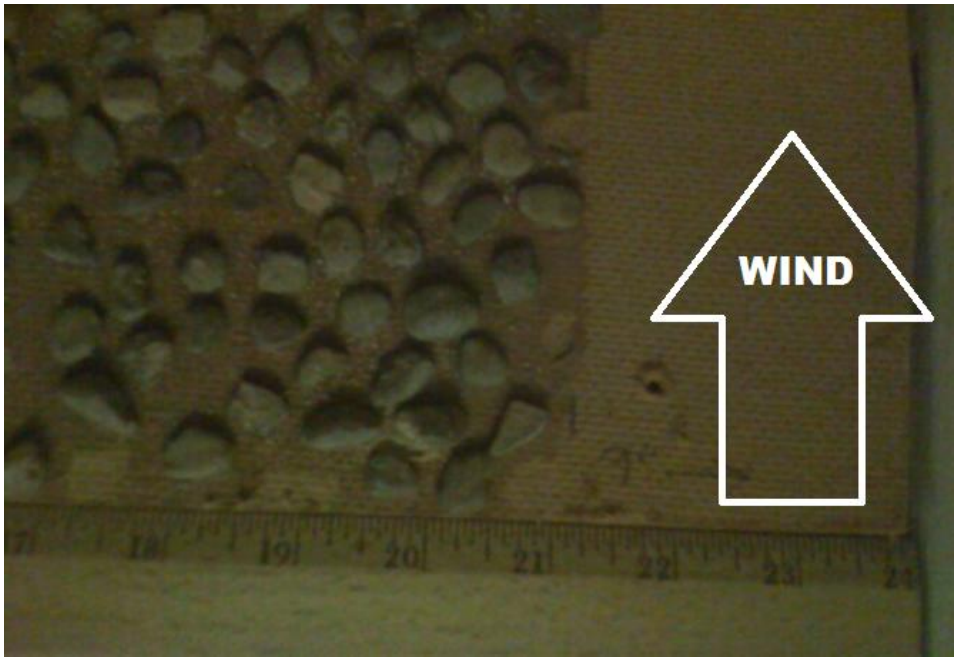

Figure 4.2: Boundary Layer Trip Device in MARSWIT Tunnel.

FLUENT has the ability to simulate the roughness height and roughness constant parameters through empirically-derived formulas based on roughness function and law-of-the-wall modified for roughness. Before those values can be assigned to a trip element in the CFD, an interface with the appropriate dimensions must be integrated and gridded in GAMBIT to slow and thicken the boundary layer after the inlet. In order to accomplish this, virtual surfaces were incorporated in the model to allow specific values of both roughness height, which determines how tall the elements are with respect to the flow, and non-dimensional roughness constant, which determines the hydraulic regime and orientation of spacing between elements. $K_s^+ \leq 2.25$ equates to hydraulically smooth, $2.25 < K_s^+ \leq 90$ gives rise to a transition region, and $K_s^+ > 90$ is considered to be fully rough.

It was assumed for initial modeling that the mean velocity distribution along the walls, when plotted in the usual way against a semi-log scale, would give an overall slope of 1/k, k

=0.4187, and an intercept of 0.5 = ΔB [34]. With an equation for actual roughness constant (C_S), as required by the code, for the boundary layer trips given as (with C_μ=0.09) [10]:

$$C_S = \frac{e^{\Delta B k} - 1}{K_S^+} \qquad (4.1)$$

$$K_S^+ = \frac{\rho K_S (C_\mu^{\frac{1}{4}} k^{\frac{1}{2}})}{\mu} \qquad (4.2)$$

Having an accurate value for C_s and roughness height is critical not just for the trips, but also for the entire floor of the inside of the tunnel, as those parameters directly affect the shear through the lower regions of the flow (assuming the "no slip" condition at the tunnel floor). Specifically, since the floor is covered in 60 grit sandpaper, a roughness height of approximately 265-269 microns (267 micron average) is reported in the literature [22]. The two values, taken together, create a boundary layer at 6.0-6.3 m at the test section that is approximately 200 mm thick, as seen in Chapter 6, Figure 6.1, displaying MARSWIT's velocity profile.

4.1.3 Meshing and Y+

In addition, at MARSWIT's observed area six meters down-stream from the inlet, a combination of layers was present in the boundary layers. As deduced by Prandtl and Kármán, expressions can be utilized to model the boundary layer (BL) as a very thin, viscous layer, a transition "buffer" layer, and a developed turbulent layer as seen in a plot of dimensionless velocity (u^+) versus dimensionless wall distance (y^+). The equation for y^+ is:

$$y^+ = \frac{\sqrt{\rho * \tau} y}{\mu} \qquad (4.3)$$

where variables are as previously defined. FLUENT models this BL as a log-law relationship when y+ > 11.225.

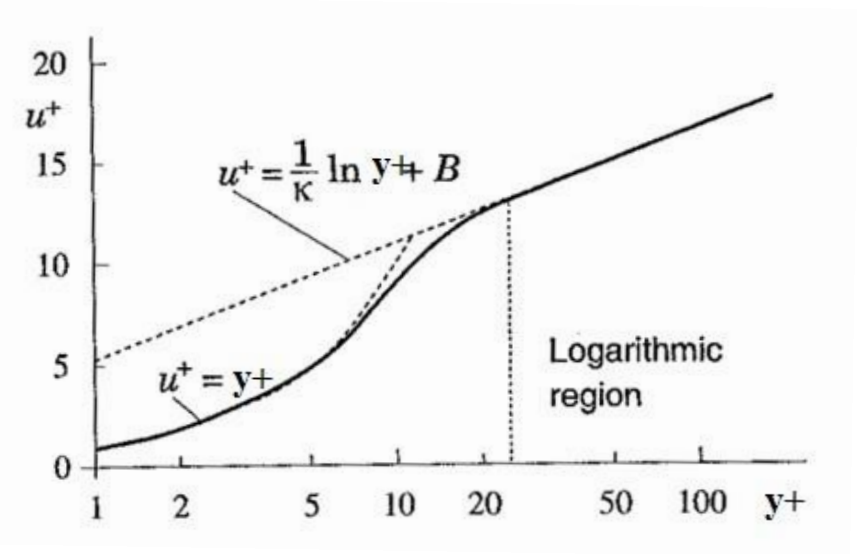

Figure 4.3: Typical Linear-log Profile Showing Transition from Laminar to Turbulent Flow. [34]

Using these values and the properties of the flow, it was possible to choose a distance, normal to the solid surface of the floor, at which the dimensionless wall distance was either < 5 or > 30. At a value < 5, the first grid data point is placed within the viscous, sub-laminar layer, which even fully turbulent boundary layers have [33]. The models used in this thesis have a dimensionless wall distance of ~2, meaning the actual velocity profile node-data is used to compute the shear on the gas-phase and particle-phase. If, however, this author were to have changed the GAMBIT model to coarser mesh spacing, and dimensionless wall distance could become > 11.225, then FLUENT would impose the standard log wall function profile from Launder and Spaulding, based on Prandtl's original boundary layer region overlap theory [34] to derive the estimated velocity values between the floor and wall function limit.

4.2 FLUENT Modeling

4.2.1 Overview

Once satisfactory modeling of the flow field had been achieved, a Discrete Phase Model (DPM) was utilized to simulate particle trajectories numerically. DPM with the Euler-Lagrangian scheme was employed, treating the particles as spheres and tracking each particle at

its center. The particles were assumed to have no volume and to interact with wall boundaries via perfectly elastic collisions [34].

4.2.2 Coupling Effects

During the course of the simulations, CFD runs with coupling modes on were compared to runs where coupling was off, and no deviations or differences in trajectories were noticed. Therefore, it was determined from observation that coupling was not an important parameter for analysis. Reasons for this could have been that the mass-loading or wind-loading factors were not sufficiently high for particles to affect each other in flight, and particles did not sufficiently bleed air momentum for unsteady effects to present themselves.

4.2.3 Residuals

3D flow, with double-precision, was used in FLUENT due to the difference in modeling 2D versus 3D airflow. In 3D flow, because airflow is typically able to move in the extra dimension afforded it over 2D, the separation point tends to be further behind the leading edge of objects like smooth spheres present in the flow than it would be in 2D flow [5]. Consequently, the expected force per unit length should be much lower, and the difference deserves the additional computational resources, as it can become significant in the final analysis.

A 1^{st} Order Discretization scheme was chosen for our results, as 2^{nd} Order Discretization results showed no observable difference and necessitated increased computing resources. What is meant by discretization is, when the flow field is gridded in GAMBIT, the field is only solved for grid points at discrete points in the flow [5]. A Taylor series expansion is written about these points where exact solutions have two components: the forward difference and the truncation error, and only the approximation to this exact solution is carried on (the forward difference). The error introduced by discarding the truncation error is steadily reduced until the solution converges below its residual value. The forward difference discretization technique is accurate in each direction to the first power, and so is named 1^{st} Order Discretization [5].

The scaled residual values after iterations presented the same trade-off in terms of solution accuracy, and comparison between a residual value for converged solutions of between

0.001 and 0.000001 did not show any meaningful differences. However, scaled residual cut off values of 0.000001 were used for all trajectory simulations presented since it is standard practice for publication, as it ensures more-accurate results.

4.2.4 Limitations

4.2.4.1 Particles as Streams

FLUENT documentation implies that the point-properties that exist in real data from NASA Ames would take orders of magnitude more computational time to calculate, given current algorithms. Instead of calculating millions of point-properties, what FLUENT does inside the program is search for all like-property clusters of particles near a point to locally model as a stream. Like-property grouping means the processor can allocate fewer resources to deliver the next cell the data it needs to continue to converge the solution. For the four representative cases, the individual injections presented to the flow were singular streams, so FLUENT's like-property streams present no difficulty for interpretation of results. The streams can be considered particles for all practical purposes [34].

4.2.4.2 Particle Injections

As per Equation 3.24, the typical speed that a particle begins movement from a static condition is the static threshold wind speed. It is unfortunate FLUENT was not able to generate numerically stable solutions to solve for these values, so calculations on initial conditions for the MARSWIT cases were performed to determine the vector components of velocity required to reproduce the results in the wind tunnel for Earth. After the values were calculated, injections of single particle streams in FLUENT were given those initial conditions to replicate trajectories.

4.2.4.3 Particle Bounce

Particles have complex interactions with any boundaries they interact with (even other particles in flight), and the resultant energy these particles retain is hard to characterize in practice. For our results, particles were assumed to have no volume [34] and interact with wall boundaries dependent on a parameter called Coefficient of Restitution as FLUENT uses it, which

determines simply the elasticity of the particles in question. FLUENT default for particle elasticity is perfectly elastic, Coefficient of Restitution = 1, meaning that a particle left a surface boundary with just as much energy as it arrived with. Figure 4.4 below shows the coefficient in terms of velocity ratios before and after a collision.

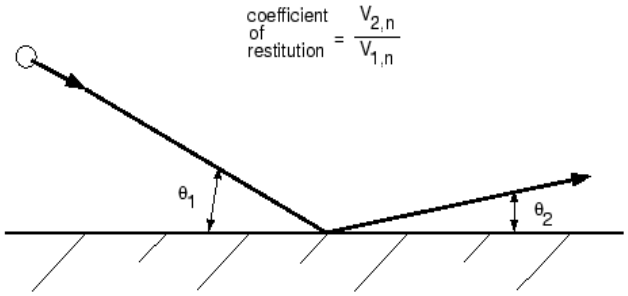

Figure 4.4: Coefficient of Restitution Definition. [34]

4.3 Approximation and Implementation of Fluid Mechanics Principles

4.3.1 FLUENT Treatment of Navier-Stokes Equations

The method employed to render the Navier-Stokes equations tractable so that FLUENT can efficiently compute solutions to systems was the Reynolds-averaging Navier-Stokes (RANS) method. Two additional terms in the form of transport equations were needed in addition to the normal equations to enable closure of the equation set.

The closure model chosen for this thesis is k-ε, where time-averaging occurs as replacements in the instantaneous Navier-Stokes equations to allow for turbulent fluctuations. For x-direction velocity:

$$u_x = \overline{u_x} + u_x' \qquad (4.4)$$

where $\overline{u}_x$ and u_x' are the mean and fluctuating velocity components in that direction [34]. The Reynolds-averaged momentum equations can then be written as Equation 3.6 (Continuity), and in Cartesian tensor notation, the Navier-Stokes equations in RANS become (i=1, 2, 3):

$$\frac{\partial}{\partial t}(\rho u_i) + \frac{\partial}{\partial x_j}(\rho u_i u_j) = -\frac{\partial p}{\partial x_i} + \frac{\partial}{\partial x_j}\left[\mu\left(\frac{\partial u_i}{\partial x_j} + \frac{\partial u_j}{\partial x_i} - \frac{2}{3}\delta_{ij}\frac{\partial u_l}{\partial x_l}\right)\right] + \frac{\partial}{\partial x_j}(-\rho\overline{u_i' u_j'})$$

(4.5) [34]

where δ_{ij} is the Kronecker delta. Equations 3.2 and 4.5 are the Reynolds-averaged Navier-Stokes (RANS) equations. They have the same general form as the instantaneous Navier-Stokes equations, with the velocities and other solution variables now representing ensemble-averaged (or time-averaged) values [34].

Additional terms now appear that represent the effects of turbulence. These Reynolds stresses, $-\rho\overline{u_i' u_j'}$, must be modeled in order to close Equation 4.5.

The Boussinesq hypothesis [5] relates the Reynolds stresses to the mean velocity gradients:

$$-\rho\overline{u_i' u_j'} = \mu_t\left(\frac{\partial u_i}{\partial x_j} + \frac{\partial u_j}{\partial x_i}\right) - \frac{2}{3}\left(\rho k + \mu_t\frac{\partial u_k}{\partial x_k}\right)\delta_{ij} \qquad (4.6)$$

where μ_T is turbulent viscosity. The advantage of the approach is the relatively low computational cost associated with the computation of the turbulent viscosity, μ_T. In the case of the k-ε model, two additional transport equations (for the turbulence kinetic energy, k, and the turbulence dissipation rate, ε, are solved, and μ_T is computed as a function of k and ε. The disadvantage of the Boussinesq hypothesis as presented is that it assumes μ_T is an isotropic scalar quantity, which is not strictly true, for example, in highly swirling flows [34], which, for this thesis, a high-swirl assumption does not apply.

4.3.2 FLUENT Treatment of Nonspherical Particle Drag

The value of the coefficient of drag depends on the particle shape and on the particle Reynolds number. For the 175-250 micron walnut shell particles used in the MARSWIT experiments, Re is calculated to be ~70, leading to the conclusion that the flow around smooth, spherical, idealized particles will behave in a laminar fashion, with earlier separation and

possibly more drag than the turbulent case for the same particles (ie. aspherical particles with irregular surfaces). However, it is also possible for highly shaped particles to have sharp turns in the local flow around them, which will tend to separate the flow earlier than it would for spheres.

For our results, it was assumed particles used are spherical particles, unless applying ϕ. FLUENT employed the drag law of Morsi and Alexander for particles with non-spherical ϕ. As the default drag law in FLUENT's Discrete Phase Model (DPM), FLUENT's spherical and non-spherical drag laws divide the particle Re ranges into eight separate sections with three coefficients, which all depend on the particle Re range described in the model [25]. In the following formula, $K_1 = 46.50$, $K_2 = 116.67$, and $K_3 = 0.6167$ for our particle Re range of interest, $10 < Re_p < 100$.

$$Spherical\ C_D = \frac{K_1}{Re_p} + \frac{K_2}{Re_p{}^2} + K_3 \qquad (4.7)$$

The equation to calculate non-spherical C_D is changed to account for the non-spherical nature of the particles according to the method of Haider and Levenspiel [15].

$$Non - spherical\ C_D = \frac{24}{Re_{SPH}}(1 + b_1 Re_{SPH}{}^{b_2}) + \frac{b_3 Re_{SPH}}{b_4 + Re_{SPH}} \quad (4.8)$$

In the formula, Re_{SPH} is the Re number of the equi-volume spherical particle referenced in the numerator of the shape factor equation. The coefficients, b, are all dependent on the shape factor for their values:

$b_1 = \exp(2.3288 - 6.4581\phi + 2.4486\ \phi^2)$
$b_2 = 0.0964 + 0.5565\ \phi$
$b_3 = \exp(4.905 - 13.8944\ \phi + 18.4222\ \phi^2 - 10.2599\ \phi^3)$
$b_4 = \exp(1.4681 + 12.2584\ \phi - 20.7322\ \phi^2 + 15.8855\ \phi^3)$

The input diameter value in FLUENT applies to the smaller surface area particle in the trajectory calculation [34], so with this information, while knowing the volumes are equal and the density is constant for the particles, it is possible to obtain the mass FLUENT used for its Lagrangian trajectories.

Chapter 5

Methods and Procedures

An experiment is a question which science poses to Nature, and a measurement is the recording of Nature's answer.

– Max Planck [*Scientific Autobiography and Other Papers*, 1949]

5.1 Analytical

5.1.1 Knudsen Number

In the modeling, the first parameter ascertained after Reynolds number was verification of continuum flow for these very small particles via computation of the dimensionless Knudsen number (Kn). Using the equations and methodology presented earlier, Kn = 0.000308 for Earth, which is <<0.001, and shows full continuum flow in the test section with respect to the particles [33]. For Titan, Kn was calculated to be 0.0000303, and also shows full continuum flow, based on the flow regimes shown earlier.

5.1.2 Reynolds Number

5.1.2.1 MARSWIT Tunnel

The first practical step in modeling a physical system like the MARSWIT atmospheric boundary layer wind tunnel is to generate and replicate the values of several commonly used variables which strongly influence the flow field. Measured pressure of 102.142 kPa was utilized for the MARSWIT CFD runs at ambient since the actual tunnel was open to its surrounding pressure. However, since temperature deviated from standard day and is estimated to have been 295.2 K, the operating density (ρ) was calculated to be 1,205 kg/m^3 and leads to a change from standard day dynamic viscosity to a new value of ~1.848E-5 kg/m-s. Dynamic viscosity for air varies strongly with change in temperature, as calculated using Sutherland's formula [11]:

$$\mu = \mu_o(0.555 * T_o + C/0.555 * T + C)(T/T_o)^{3/2} \qquad (5.1)$$

$\mu = viscosity\ at\ T,\ \mu_o = viscosity\ at\ T_o, and\ C = Sutherland's\ Constant\ for\ air = 120.$

The calculation for the MARSWIT tunnel, given its characteristic length of 1 meter and speed in the test section for typical run ranges, yields Re = ~323,340 and places the flow in what should be a fully-developed, fully-turbulent regime. For Titan runs in the model, Jose Aliaga-Caro, part of the Titan team, determined dynamic viscosity of the atmosphere for Titan with a partial pressure formula, since the relative composition of Titan's atmosphere is known [26]. The value of 8.02564E-6 kg/m-s is the value used for our results, and has been verified by Kok [35]. Re using this value was calculated for the slowest airspeed case we have, 1.35 m/s, and at ~900,000, our model should present fully turbulent flow with trips.

$$Re = \frac{\rho V D}{\mu} = \frac{5.3446 * 1.35 * 1}{8.02564E - 6} = \sim 899{,}020$$

5.1.2.2 MARSWIT Particle

For particles like walnut shells with a nominal diameter of 213 microns, Re_p is on the order of 68.87 using relative velocity difference, which will be used in calculations for particle

drag. Because the modeling and real world values for velocity are comparatively small for compressibility effects, compressibility of air at these speeds will be considered negligible.

5.1.2.3 Titan Particle

Titan particle Re calculation is similar to the Earth case, and Titan's atmosphere, composed of mainly nitrogen, behaves very much like Earth's. Using the same values for atmospheric density for Titan, 5.3446 kg/m3, and dynamic viscosity as before, and nominal particle diameter of 500 microns, Re was calculated at 0.8 m/s relative velocity difference to give Re_p = ~266.

5.1.3 Hydraulic Diameter and Turbulence Approximation

As the methodology discussion in Chapter 4 indicated, use of Equation 3.13 to 3.15 give, for the MARSWIT Wind Tunnel on Earth, a hydraulic diameter (D_H) of 1.096719 m. A value 3.27% turbulence intensity was calculated, and is reasonable, indicating the flow should be ordered and well-structured at the inlet. Turbulent length scale results in ℓ = 0.07677 m, when paired with the hydraulic diameter. With I, ℓ known, k and ε values used for our results for the two-equation turbulent model were found to be:

$$k = \frac{3}{2}(u_{avg}I)^2 = \frac{3}{2}(5 * .0327)^2 = 0.040098$$

$$\varepsilon = (C_\mu)^{\frac{3}{4}} * \frac{k^{\frac{3}{2}}}{\ell} = (0.9)^{\frac{3}{4}} * \frac{0.040098^{\frac{3}{2}}}{0.07677} = 0.096645$$

5.1.4 ImageJ Particle Tracking

5.1.4.1 Noise and Particle Resolution

The Phantom v12 camera used in the data collection runs at NASA Ames is capable on the extreme end of capturing 1,000,000 frames per second (fps). Data were taken at 120 micro-second exposure and only 1000fps and 344x512 pixels, so higher resolutions in the future could be obtained while simultaneously satisfying hard-drive constraints with computing resources

available during the runs. Once either the recording drives get larger or the run sample video is limited to smaller test lengths, one can increase both the resolution to approximately 1280x800 pixels and ~6000fps. In essence, one can more than double the spatial resolution and use the better position and time data to more accurately determine the particle location and velocities during the run.

5.1.4.2 Trajectory Curves

Particle video data were obtained using a Phantom v12 high-speed digital video camera at approximately 1000 frames per second, where the camera focal plane was set so that a 2D slice of the downstream flow could be viewed with particles in focus while "in-plane." ImageJ software was then used to process each run to convert pixels (particles) and centroids to x-y data which could then be compared to FLUENT output. Figure 5.1 illustrates the use of ImageJ in the frame-by-frame tracking of particle trajectories. To date, this work has provided time histories of particle position, velocity, and flight direction for approximately 100 particles under known free stream conditions. These saltation data were then culled for usable runs where trajectories were clearly seen apart from the chaotic flow near the bottom, where particle identification was difficult.

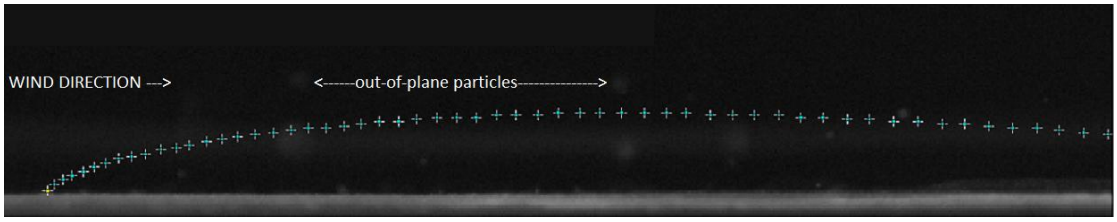

Figure 5.1: Tracking of Walnut Shell Particle in Fully Turbulent Flow at 5.45 m/s.

During each frame advance, the x and y location was also marked on the screen, leaving the blue trail of positive symbols across the screen. Fuzzy "blobs" in the background of Figure 5.1 are labeled as out-of-plane particles that were not in focus during their transit of the camera's Field of View (FOV). Wind direction as indicated was from left to right.

5.1.5 Calculating Robins-Magnus Force Effect Correction

After careful coordination with Ansys, the makers of FLUENT, it was discovered that (apart from Saffman lift forces for sub-micron particles), FLUENT has no native ability to model particle torques, moments due to boundary interactions, or any spins capable of causing significant pressure differentials or Magnus lift forces. After considering the x-y position results obtained after correcting trajectory due to sphericity, it was decided to manually apply the formulation for Magnus force due to anticipated spin direction and magnitudes and incorporate those forces into the y-component direction (in addition to the gravitational body force). The only other forces possibly affecting trajectory apart from this would be particle-particle collisions, but, due to the low mass-fraction of walnut shells in the air, this effect has to be considered negligible for now.

Using values calculated from Chapter 3's explanation and methodology for Magnus force, a correction due to Magnus effect can be determined, and because density and volume of the particles are known, so mass can be calculated. Using F=ma, a corrective acceleration was determined, and this correction was subtracted (up direction) from the "down" direction gravitational acceleration (-9.81 m/s^2 for Earth and -1.35 m/s^2 for Titan) used in FLUENT. Particle mass is approximately 5.394303x10^-9 kg for Earth and approximately 3.05x10^-9 kg for Titan, at average values of 213 and 180 microns, respectively.

Kok [17] identifies two possible sources of torque, inducing a spin, for particles in saltation: displaced contact force from where the particle hits the surface, and a shear induced force as the particle interacts with the flow velocity gradient. Due to these forces Kok estimates particle spin rates (referencing Loth) on the order of 500 rev/s [17][21], which will suffice for our estimate for Magnus force, after converting to radians/second. There will be a brief discussion on constant spin rate impact on trajectories when varied in Chapter 6. As mentioned earlier, the next step is to determine the spin lift force coefficient by determining the non-dimensional particle angular spin velocity (Ω_{p}^{*}) which is for Earth:

$$\text{Earth } \Omega_{\mathrm{p}}^{*} = \frac{\bar{\Omega}_{\mathrm{p}} * D_p}{|\bar{v}_R|} = 0.029583$$

And for Titan is:

$$\text{Titan } \Omega_{\text{p}}^{*} = \frac{\bar{\Omega}_{\text{p}} * D_p}{|\bar{v}_R|} = 0.3125$$

By following this value calculated for Earth or Titan along the line for Re appropriate to either Earth or Titan, a value for each case's $C_{L\Omega}^{*}$ can be determined from the graph Figure 3.3 as, for Earth and Titan, respectively:

$$Earth\ C_{L\Omega}^{*} = 0.35$$

$$Titan\ C_{L\Omega}^{*} = 0.03$$

5.2 Computational

5.2.1 Setting Initial Conditions

Initial conditions for FLUENT, accessed from a drop-down menu in the Graphical User Interface (GUI), affect each case's unique starting parameters for such properties as:

1) Initial velocity and vector components
2) Inlet face for velocity
3) Injection types and velocities
4) Injection Material Type

Injection material type in FLUENT must be create from known values for items like walnut shells, which are not standard items in FLUENT's library. It is for this reason, the value for density is critical.

5.2.1.1 Matching Test Section Velocity

Matching test section velocity was an iterative procedure which entailed various attempts to identify the appropriate inlet speed which generated the correct (MATLAB) velocity during the runs at the clock time when the Case Run particle was traversing the test section. The initial velocity was often-times about 0.2 m/s slower at the inlet than in the test-section of the FLUENT runs, but even this helpful estimate only slightly helped narrow down the range for Earth.

Because the Titan velocity estimates given by Dr. Burr were substantially smaller than the values for Earth, the lowest speed in the three cases presented in this study for Titan, 1.0 m/s had to be increased to 1.35 m/s because of instability in the run's convergence. It is for this reason the slowest run is at this speed.

5.2.1.2 Determining Velocity Components

The model in this thesis does not calculate the initial particle lift off from the surface, but rather begins with a particle position and velocity derived from experimental data and propagates the particle's path forward in time. To determine the initial particle position and velocity, images from the Phantom high speed video camera were analyzed using ImageJ. To reduce noise in the hand selected particle positions and to provide a more reliable starting position and velocity for input into Fluent, the particle x and y positions were curve-fit as a function of time using 6^{th} order polynomials. X is the horizontal coordinate, with the flow moving in the positive x direction, and y is the vertical coordinate. Thus, at some starting time, these curves could be used to provide particle position, and their derivatives provided particle velocities.

For example, below one can see the process of curve-fitting and equations generated for case 21S used for the MARSWIT section of the thesis. All other cases for MARSWIT were treated in the same manner.

Case 21S:

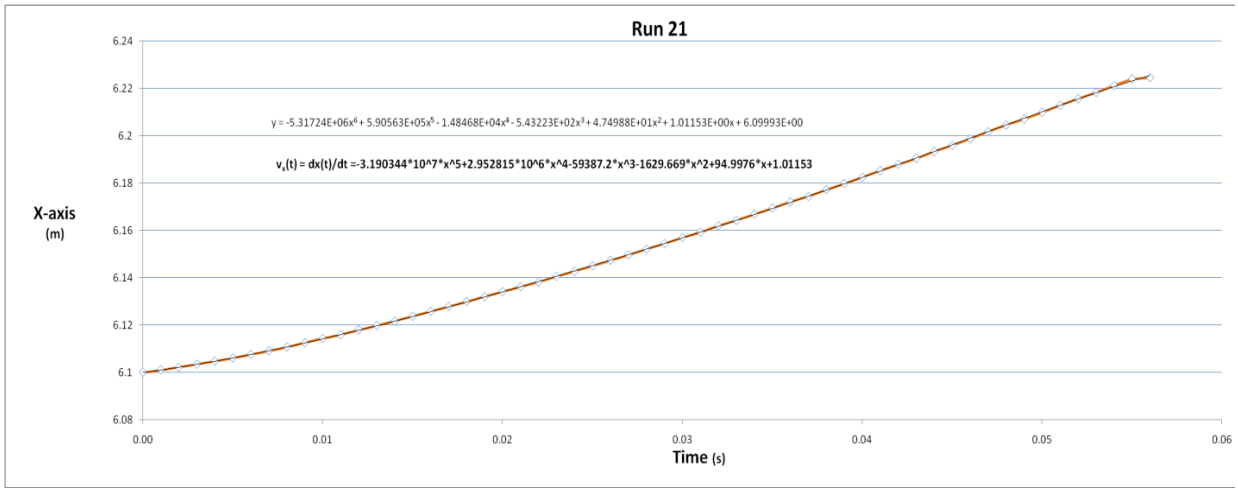

Figure 5.2: Particle x-direction Component Position versus Time Curve and Velocity Time Derivative Run 21S.

For position data in Run 21S, equation $y = -5.31724E+06x^6 + 5.90563E+05x^5 - 1.48468E+04x^4 - 5.43223E+02x^3 + 4.74988E+01x^2 + 1.01153E+00x + 6.09993E+00$ was used, and the time derivative gave $v_x(t) = dx(t)/dt = -3.190344*10^7*x^5+2.952815*10^6*x^4-59387.2*x^3-1629.669*x^2+94.9976*x+1.01153$. Similar procedures yield y-direction ("up") data for the run.

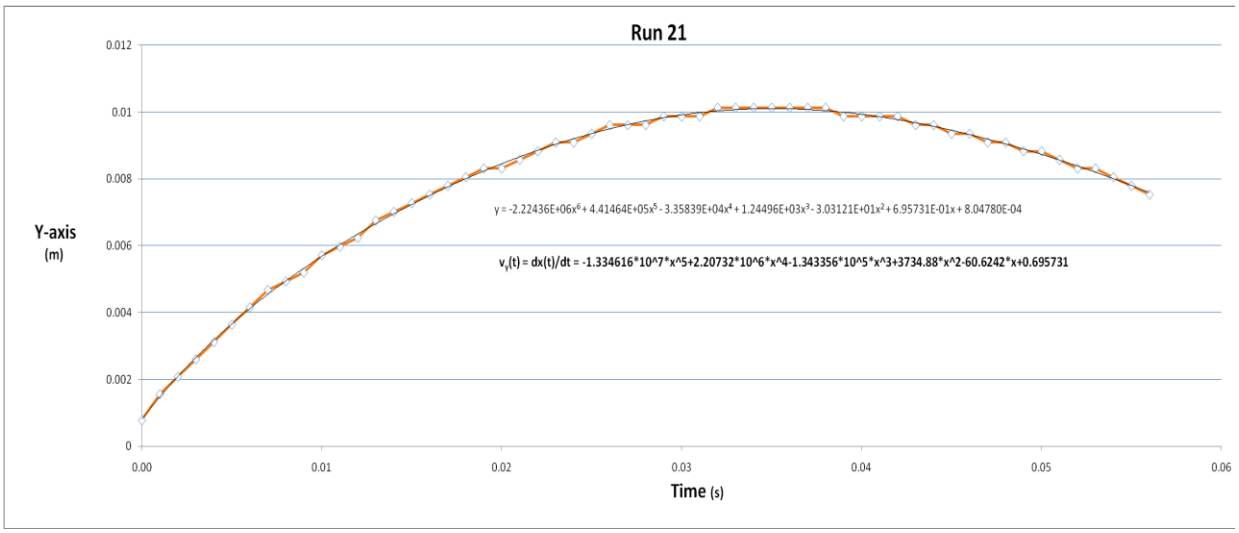

Figure 5.3: Particle y-direction Component Position versus Time Curve and Velocity Time Derivative Run 21S.

Case 21M

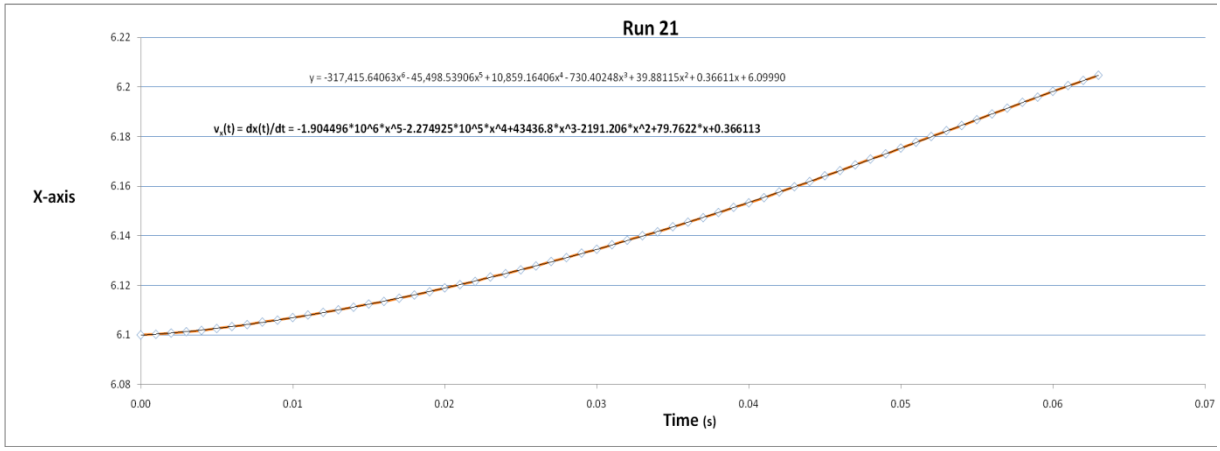

Figure 5.4: Particle x-direction Component Position versus Time Curve and Velocity Time Derivative Run 21M.

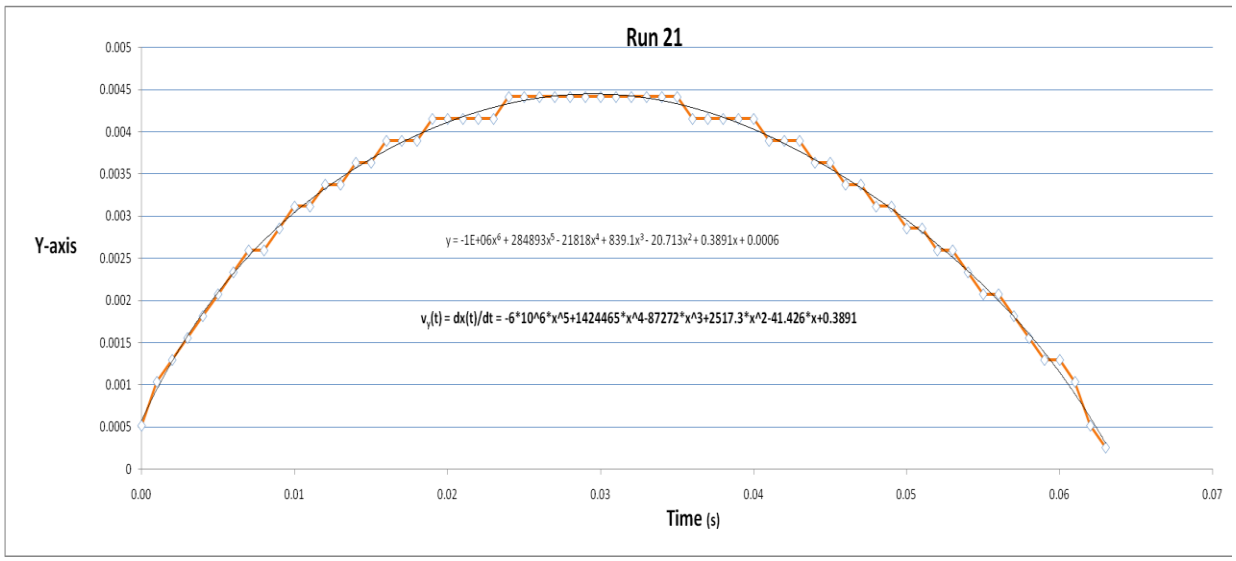

Figure 5.5: Particle y-direction Component Position versus Time Curve and Velocity Time Derivative Run 21M.

Case 23!

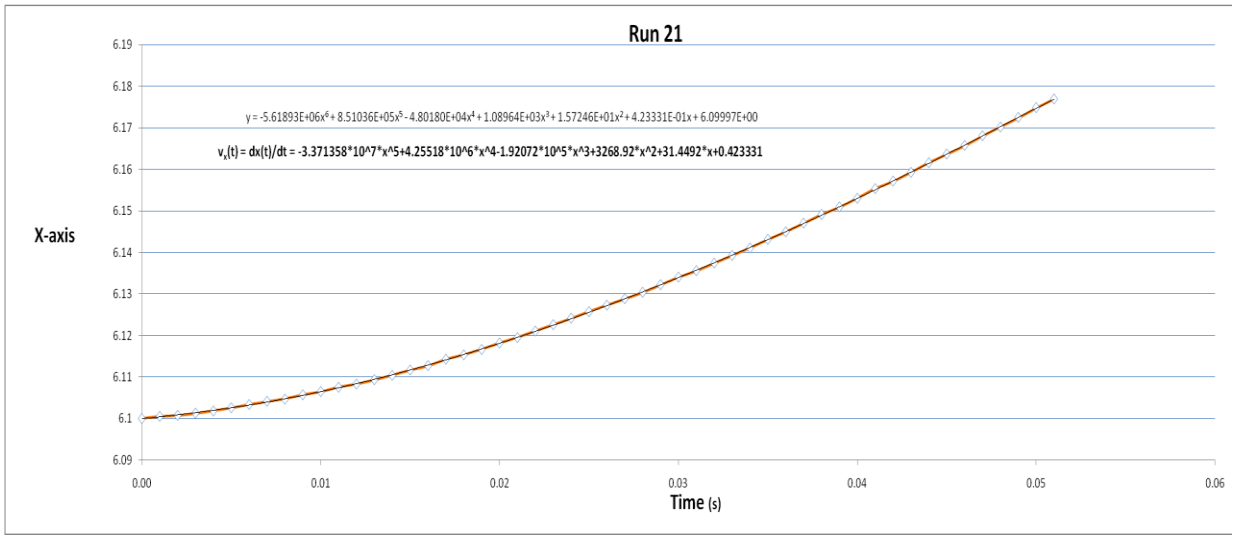

Figure 5.6: Particle x-direction Component Position versus Time Curve and Velocity Time Derivative Run 23!.

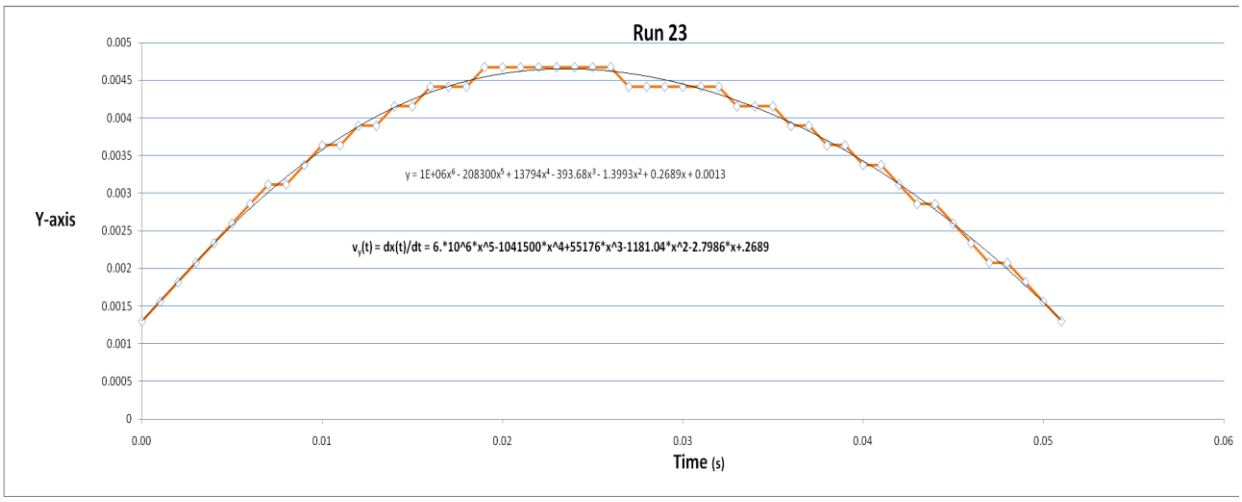

Figure 5.7: Particle y-direction Component Position versus Time Curve and Velocity Time Derivative Run 23!.

Case 23C

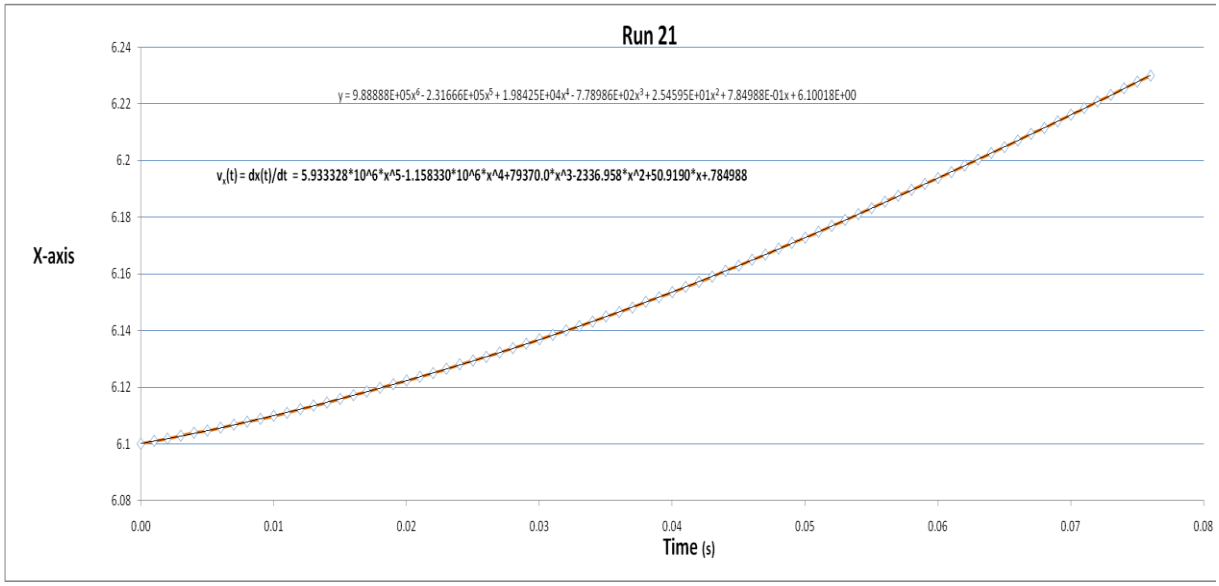

Figure 5.8: Particle x-direction Component Position versus Time Curve and Velocity Time Derivative Run 23C.

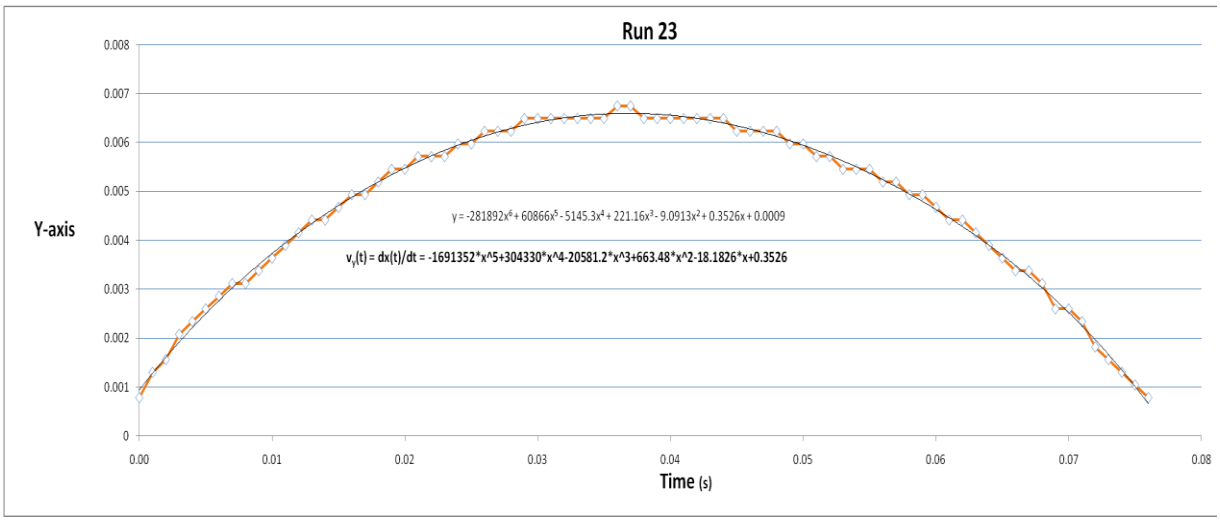

Figure 5.9: Particle y-direction Component Position versus Time Curve and Velocity Time Derivative Run 23C.

Component velocity data for Titan results simply re-used the initial condition component values for the run all the Titan runs started from, which was Run 21M. The reason for this was static threshold speed could not be replicated, but results for Titan still hold true, although a bit specifically, for the conditions where particles experience exactly the lift forces on Titan to produce the component velocities used to accelerate it from rest. For this reason, the thesis also directly compares trajectories for an Earth and Titan particle for the representative velocity on Titan and Earth where the applied particle forces, and therefore the initial velocities, are equivalent. A detailed discussion will be presented in Chapter 6.

5.2.2 Operating Conditions

The following section's principle purpose is to provide a readily available reference for the FLUENT environmental values used for Earth and Titan runs. Titan data was obtained from the Huygens Atmospheric and Surface Instrument (HASI) package aboard the Huygens probe, which spent over 90 minutes transmitting data, while on the surface of Titan [26].

5.2.2.1 Earth

In order to replicate the results from FLUENT, one would have to know the general environmental variable input values to use with each run. This section will list each variable, although most have been mentioned earlier in the Re number calculation section.

Atmospheric Pressure:	102.142 kPa
Atmospheric Density:	1.205 kg/m^3
Dynamic Viscosity:	1.848E-5 kg/m-s
Temperature:	295.2 K
Gravity:	-9.81 m/s^2

5.2.2.2 Titan

Atmospheric Pressure:	146.700 kPa
Atmospheric Density:	3.5446 kg/m^3
Kinematic Viscosity:	8.02564E-6 kg/m-s
Temperature:	93.5 K
Gravity:	-1.35 m/s^2

5.2.3 Applying Body Force Terms as Acceleration Corrections

Within FLUENT, there were provisions for general application of a body force term for the entire run. It was with this capability that the Magnus force correction was carried out by varying the standard gravity value presented in the previous sections.

The individual run values calculated with the procedure from Chapter 3 were then added to the standard values to reduce the gravitational amount across the entire length of the tunnel for all time steps in the run's solution. While this is not exactly how a particle's spin rate produces a change in lift force in real flows, this method was the only practical way to model an average effect, and to account for Magnus effect since FLUENT does not model particle spin at this time.

Chapter 6

Results, Validation, and Projections

Observations always involve theory.

– Edwin Hubble

6.1 MARSWIT Tunnel Results and Comparison to FLUENT

In MARSWIT, the raw, MATLAB file data on flow speed from the traversing and free stream pitot tubes were carefully culled of erroneous inter-position values, so that long-duration, time-averaged values for steady-state flow could be obtained. Both tipped and non-tripped traverse data was plotted, normalized with respect to the max traverse velocity. After observing reasonable agreement between FLUENT and wind tunnel data, the un-normalized, raw speeds were graphed and computed for the tripped, fully turbulent condition, so that when test section velocities for the MARSWIT matched the CFD test section at 5.45 m/s, the CFD inlet boundary condition showed a requirement for 5.00 m/s computational inlet speed for the initial run data used at NASA Ames during the summer 2010 collaboration. Figure 6.1 below shows the comparison of the CFD to real-world data, and was the data used to validate the continuum flow, allowing research progression to particles.

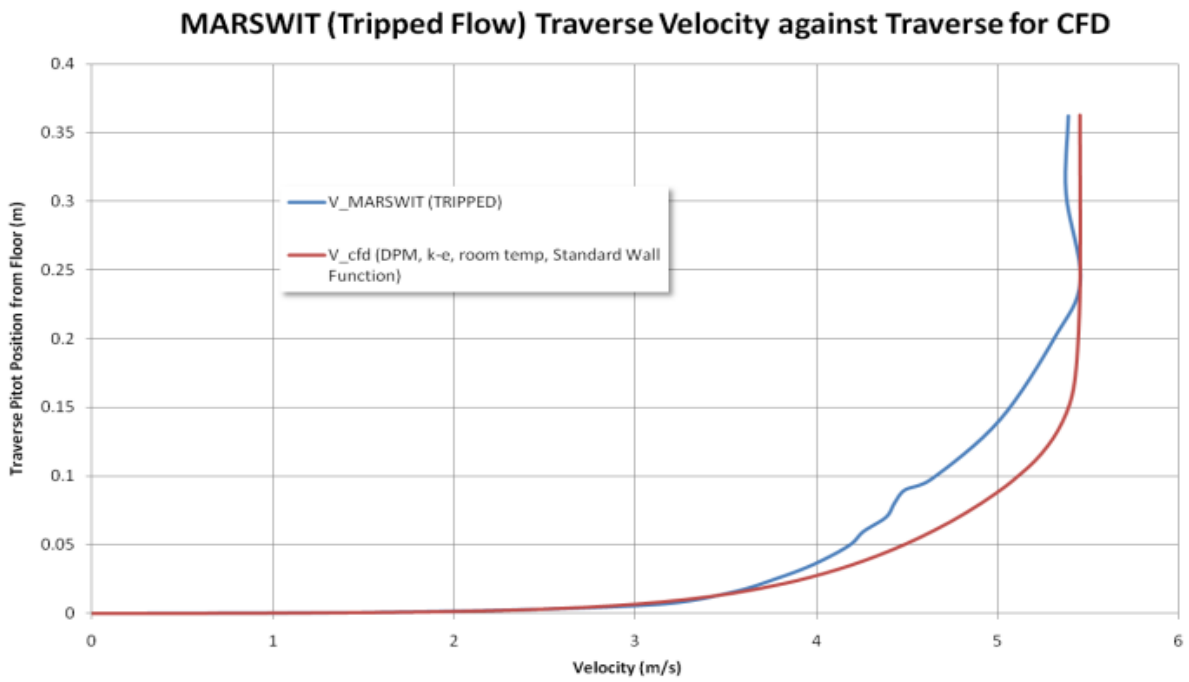

Figure 6.1: Test Section Tripped Velocity for Empirical vs. FLUENT.

The 99% free stream velocity corresponds to the top of the boundary layer thickness, and the most-critical area of modeling for trajectories is the rapidly changing near-floor velocity at y = 0.025 m. Because this is a turbulent profile, one can see the clear log-relationship downstream velocity has with respect to height above the floor [33]. This sharp increase in shear has a profound impact on initial trajectory velocities for particles departing the surface.

After particle trajectories were introduced, the research focused on shape definition and shape manipulation in the CFD, concluding with the results present at the AGU conference as discussed in Chapter 2. What was presented at the AGU meeting was that, although a sphericity of 0.4 seemed to match the data extremely well away from the initial impetus into the flow, from preliminary estimates from team member John Hills, using microscopic observation, the sphericity of the walnut shell particles was estimated to have been (initially) much closer to 0.8 or 0.9 than 0.4. Therefore, other factors must explain the shallowing of the trajectory as compared to the empirical data, or, if could be shown to be all within error bounds, then demonstrating the error limits should be the next logical objective for the research progression.

Only after that could this thesis's approach be utilized for an analysis of projected Titan trajectories.

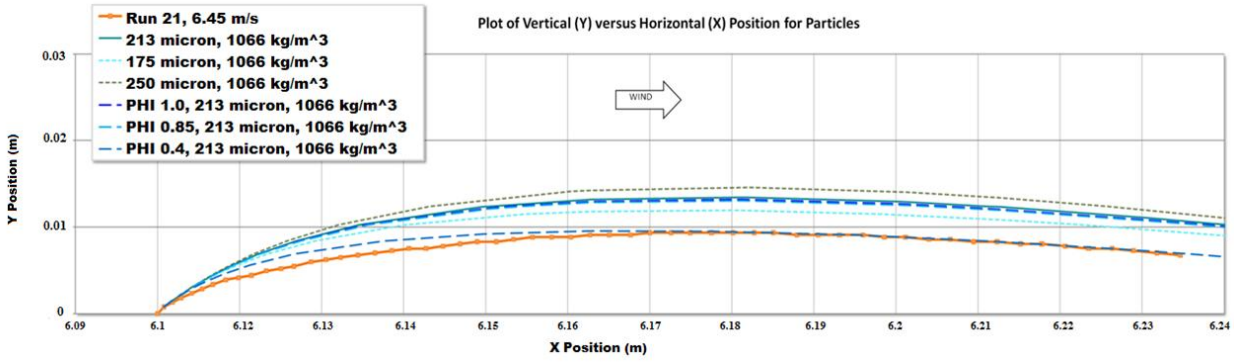

Figure 6.2: Simulated trajectories for both spherical and non-spherical particles at ρ=1066 kg/m^3.

The following sections show the work after AGU, when the research incorporated Magnus spin effects, and error analysis, and, finally, Titan results for specific initial velocity values.

6.2 Initial MARSWIT Results for Four Cases

As before, we begin the results presentation with Run 21S, where in Figure 6.3 to 6.6, the top graph shows Phi variation from 1.0 to 0.4, and the bottom graph shows the same, only with Magnus force effects factored in. Because it was not possible to know the exact Phi of the particular particle in this, or any other run, the research postulated an average Phi value which was determined earlier and set at 0.93. Discovered Phi results fell within or very near the uncertainty bounds.

Case 21S:

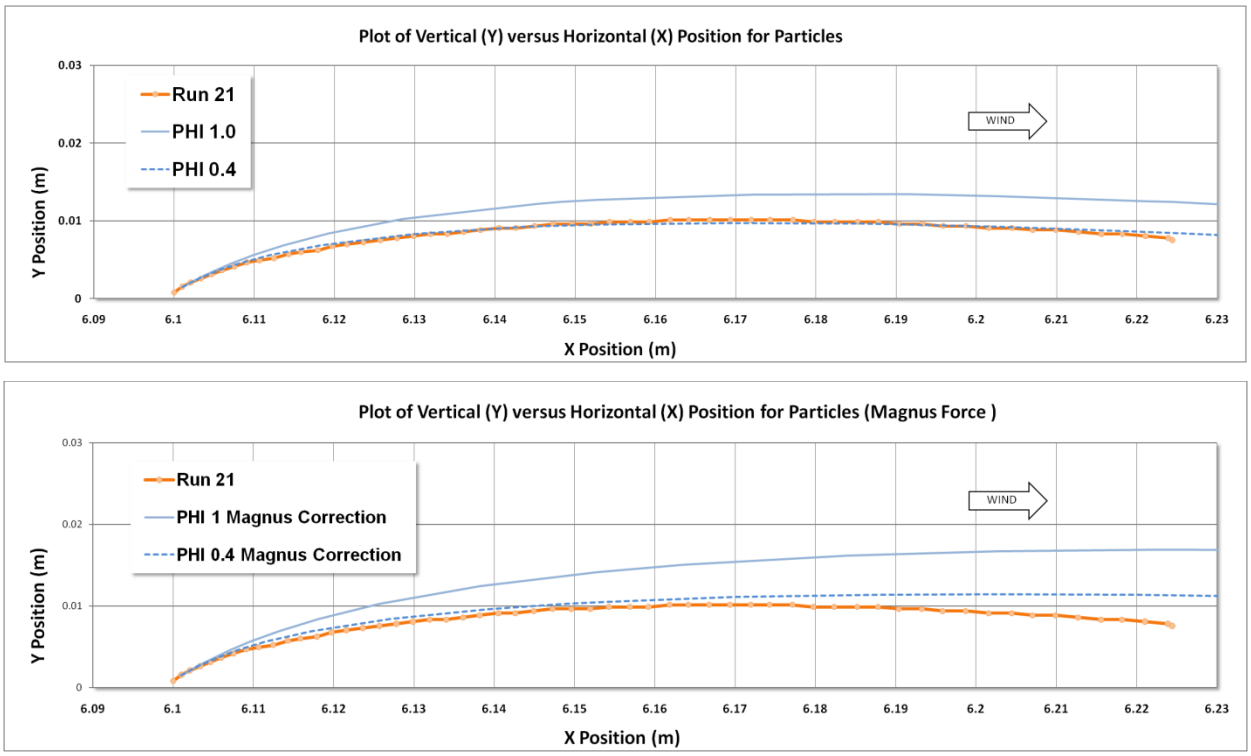

Figure 6.3: Trajectory Plots for Phi = 1.0 and 0.4 without (top) and with (bottom) Magnus Effect Run 21S.

As expected, Magnus force effects increase lift on each particle, causing the loft to increase as well. Figure 6.2 provides a view of how high a given particle could potentially loft, given a scenario where lift generated was maximized using the average of freestream velocities. The interim results show that variation of Phi to a value of 0.4 matches the original data trajectory very well, but without knowing the error bounds for this run, definite conclusions are not possible.

Run 21M below in Figure 6.3 shows a slightly different result, because both Phi of 1.0 and 0.4 are close to each other, and match the original trajectory very well. Due to this, confidence in the results was increased, but uncertainty bounds must still be demonstrated.

Case 21M:

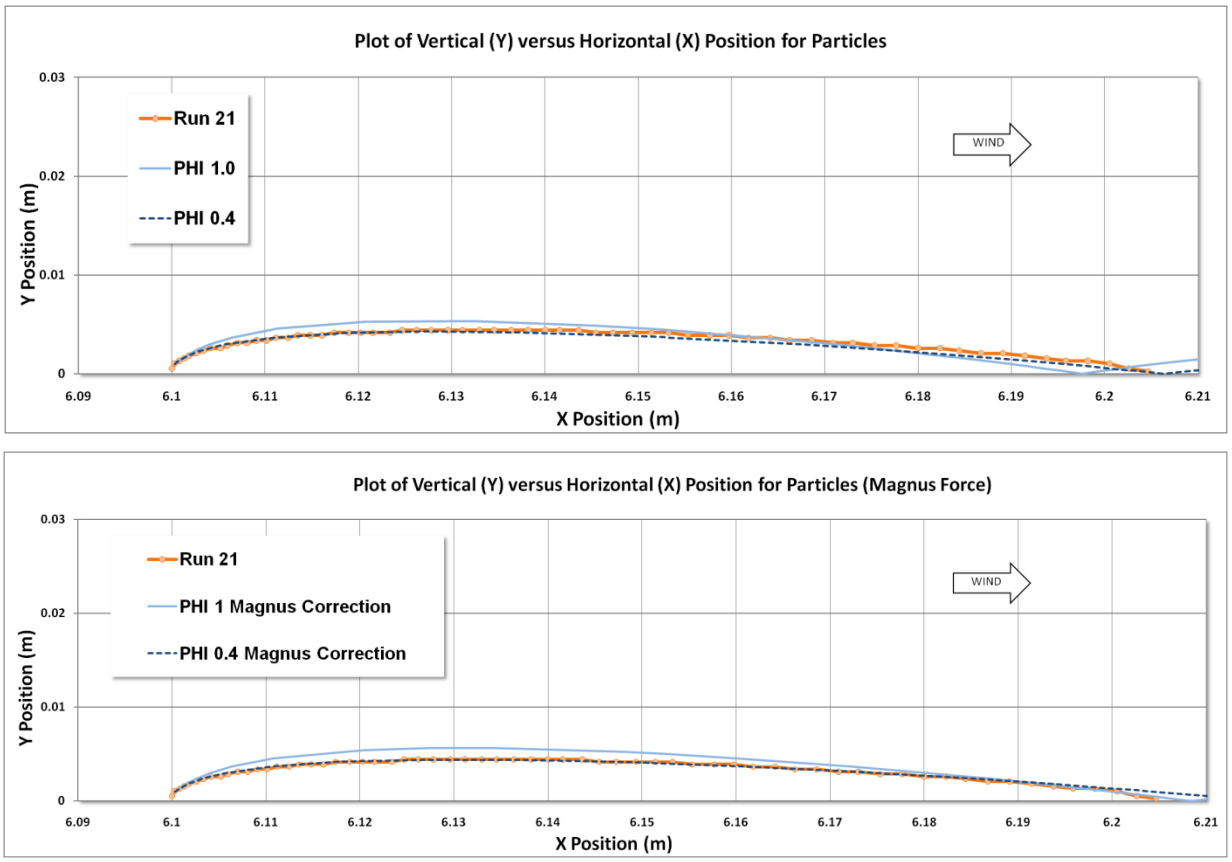

Figure 6.4: Trajectory Plots for Phi = 1.0 and 0.4 without (top) and with (bottom) Magnus Effect Run 21M.

Run 23!C is similar to Run 23M, in that trajectory data match once more. Magnus force data tends to over-loft the CFD results over the original data, but agreement is good. The top graph was not plotted with Phi = 0.4 because it was known that a lower Phi value would significantly under-loft the original data, and Phi = 1.0 (without Magnus correction) was a match.

Case 23!C:

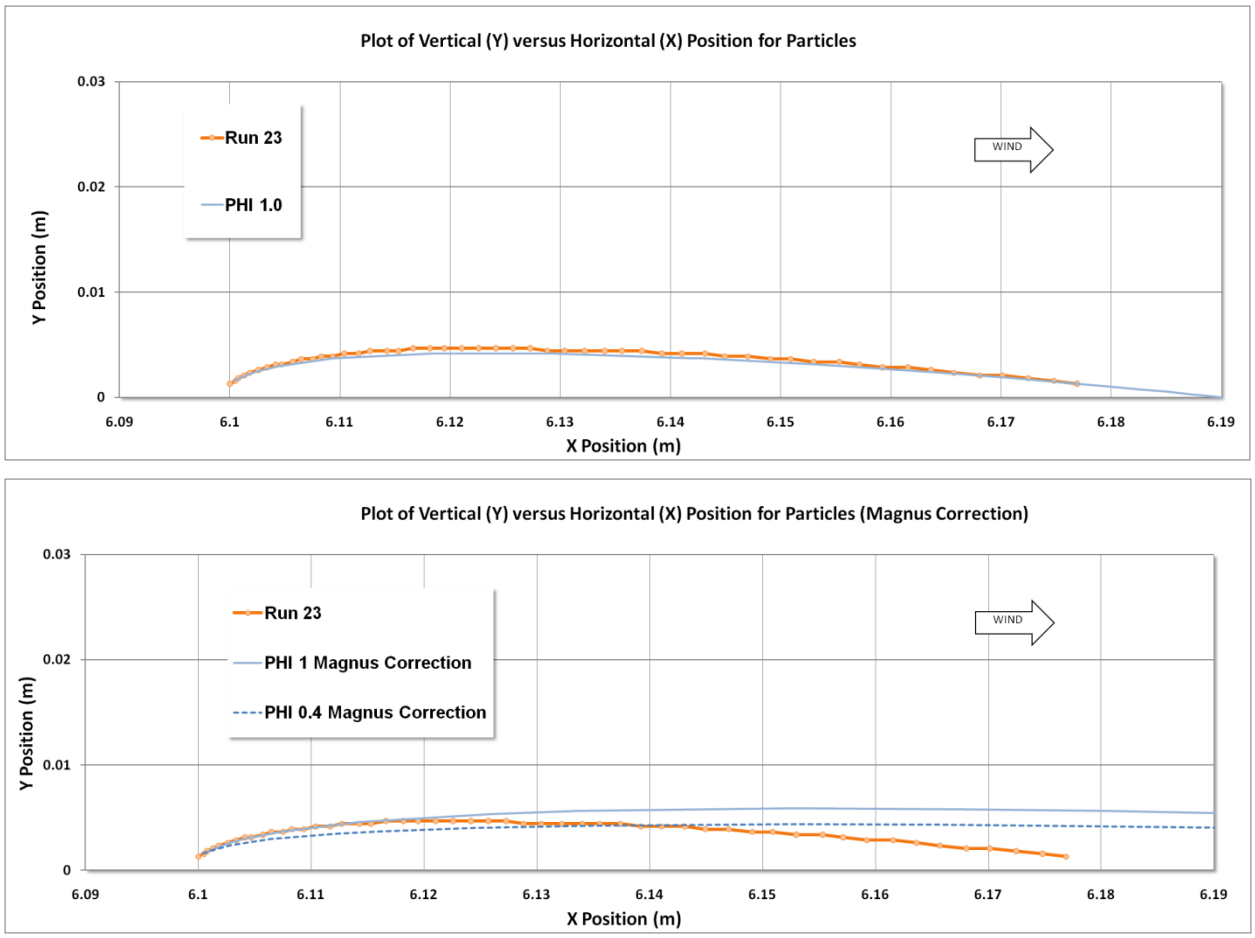

Figure 6.5: Trajectory Plots for Phi = 1.0 and 0.4 without (top) and with (bottom) Magnus Effect Run 21!C.

An interesting effect occurred in the results for the last run in Figure 6.5. Magnus correction does not over-loft the initial stages of the upward trajectory of both Phi plots, as in previous graphs. Phi of 0.4 was not plotted for the non-corrected case as it would under-loft the spherical case substantially. All plots under-predict the original data initially, but despite this, both the uncorrected case and the Magnus force plot have excellent agreement until the tail end, where constant Magnus correction keeps the trajectories high.

Case 23C:

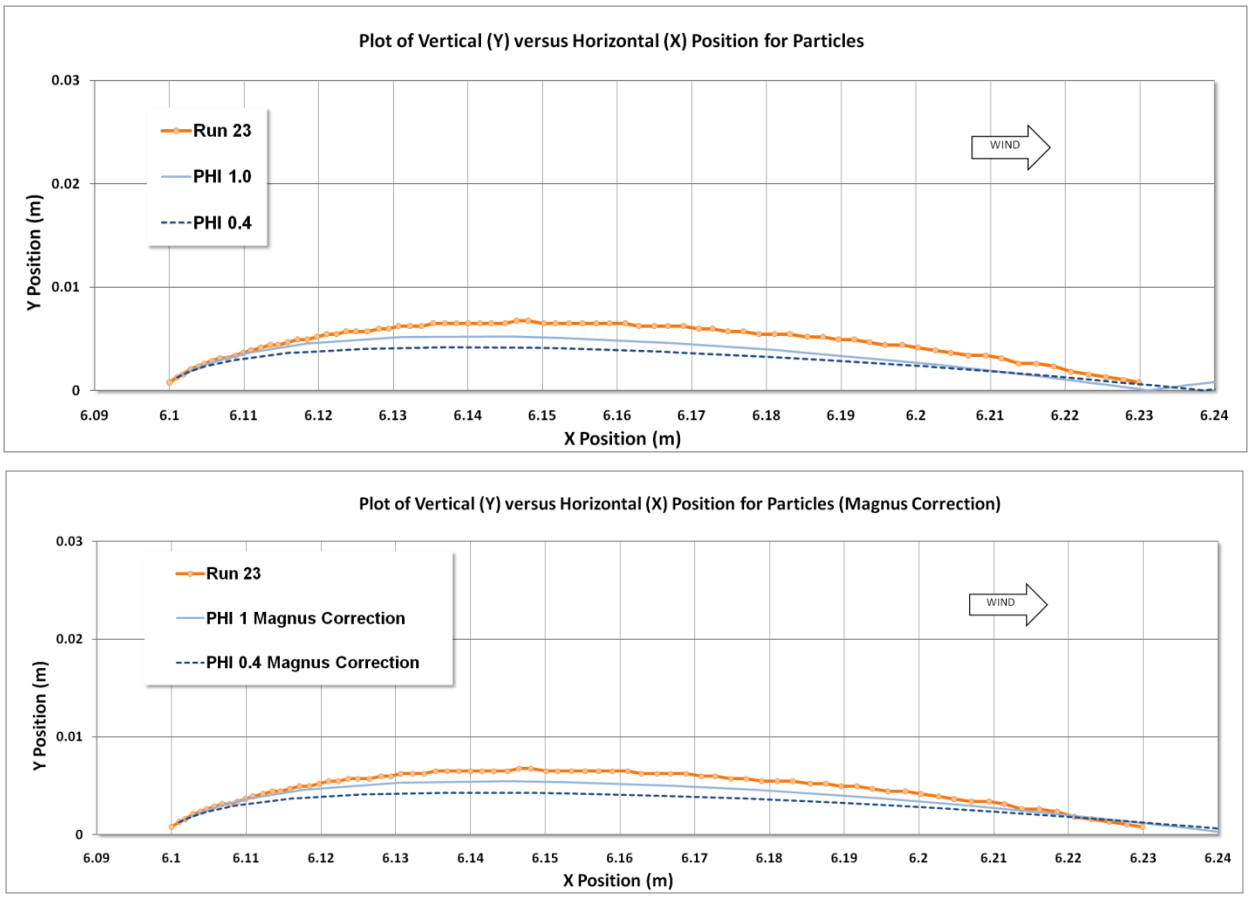

Figure 6.6: Trajectory Plots for Phi = 1.0 and 0.4 without (top) and with (bottom) Magnus Effect Run 21C.

What remains to be seen in the results is whether the plots fall within uncertainty bounds calculated by varying density and size of the particles to maximum and minimum values for each given velocity injection. Section 6.3 below presents those results.

6.3 MARSWIT Results with Uncertainty Bounds

As mentioned in Chapter 3, the error presented in determining the density of walnut shell particles has a critical effect on trajectories, and the distribution of sizes within the sieved samples in MARSWIT means there exists a possibility for a high uncertainty bound for a combination of small diameter and high density, and a low uncertainty bound combination of

high diameter and low density. Determining the variation values in Chapter 7 and Chapter 3, Table 3.2 and Table 7.1 show that particles could have ranged from as small as 175 microns, maximum density of 1,397 kg/m^3, and 250 microns at 862.7 kg/m^3. Injection values specific to each case were used in FLUENT to generate results in Figures 6.7 to 6.10.

Case 21S:

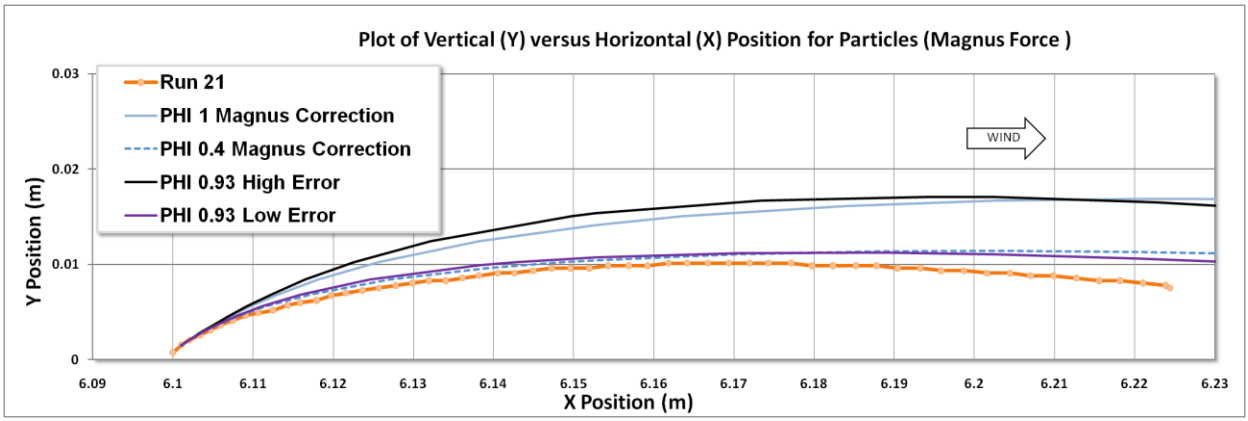

Figure 6.7: Trajectory Plots for Phi = 1.0 and 0.4 with Magnus Effect and Error Bounds Run 21S.

In Figure 6.7, high and low error bounds are presented in black and purple, at the most-likely Phi of 0.93. The results for this run show that, while Phi of 0.4 trajectories match the original data file well, we know the actual shape of the particle captured in this run is more likely to be closer to 0.93 than 0.4. What the uncertainty bounds show is that, even at the Phi value of 0.93, it is possible for a trajectory to coincide to original data quite well at the low uncertainty bound.

Case 21M:

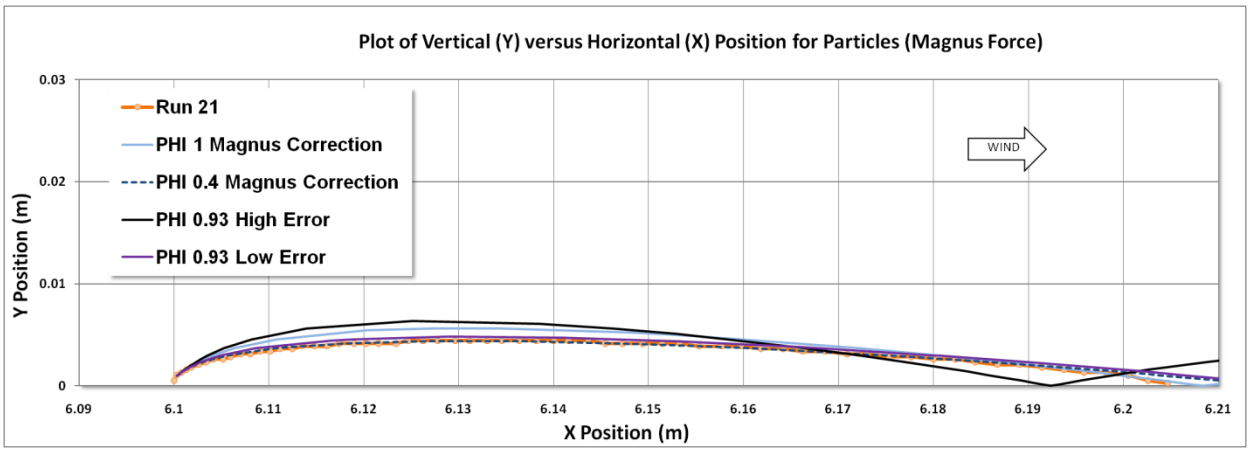

Figure 6.8: Trajectory Plots for Phi = 1.0 and 0.4 with Magnus Effect and Error Bounds Run 21M.

Figure 6.8 shows the same result as Figure 6.7 in that the low uncertainty bound corresponds to the empirical data trajectory. The high bound falls through the data from MARSWIT towards the end of the run, but the bounds again capture the dataset, and overall uncertainty pathlengths are off by less than one and one-half centimeters to the original data.

Case 23!C:

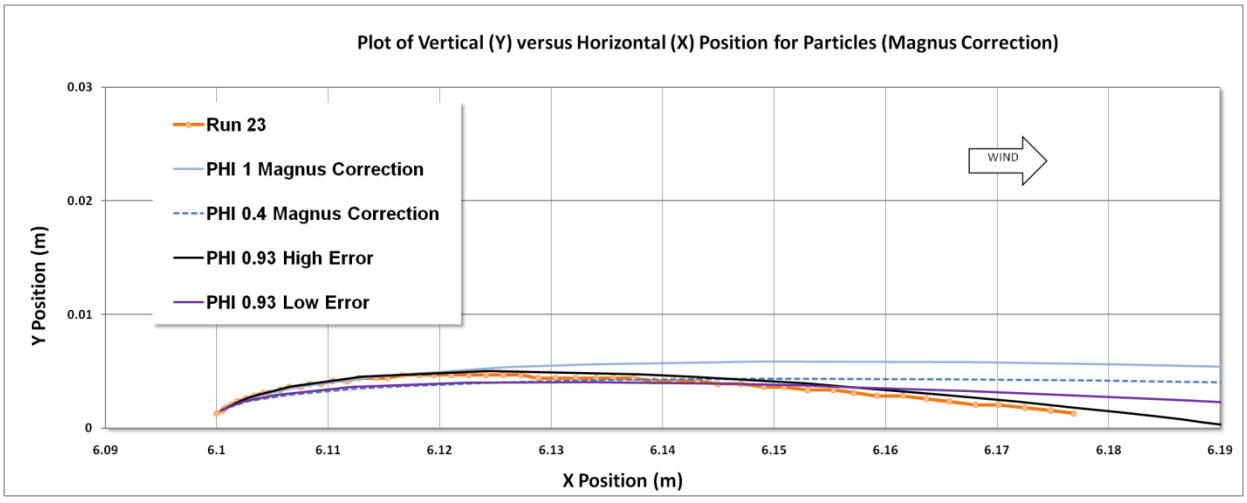

Figure 6.9: Trajectory Plots for Phi = 1.0 and 0.4 with Magnus Effect and Error Bounds Run 23!C.

In Figure 6.9 high and low uncertainty bounds straddle the dataset from MARSWIT, and bolster confidence that an accurate trajectory simulation has been made. In fact, the high uncertainty bound is nearly perfectly aligned with the MARSWIT data throughout the trajectory arc.

Case 23C:

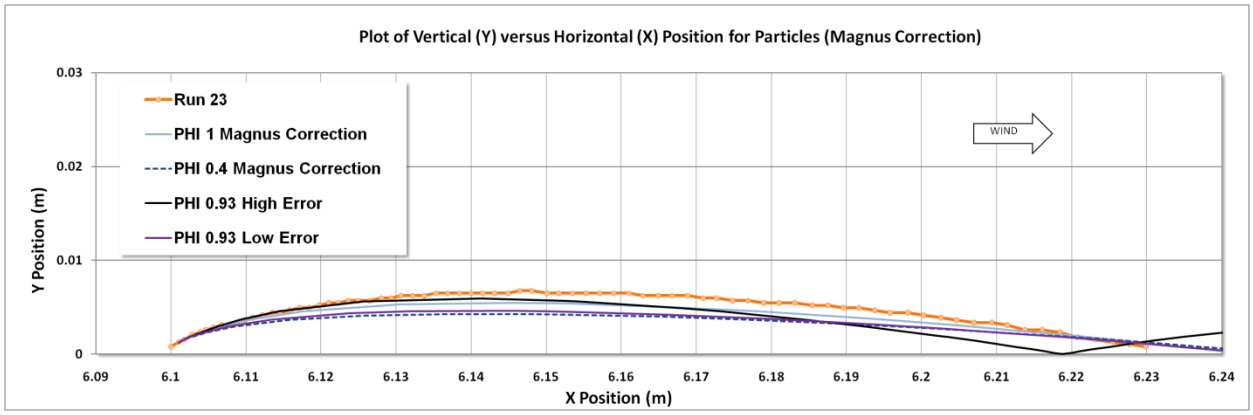

Figure 6.10: Trajectory Plots for Phi = 1.0 and 0.4 with Magnus Effect and Error Bounds Run 23C.

The last result for Run 21C is slightly outside the uncertainty bounds in terms of height, but the overall path length for the low uncertainty bound is within approximately one centimeter if the original data were to be extended with an imaginary line to the surface. On this basis, excellent agreement can be said to occur.

Overall, all four runs presented good to excellent agreement to the empirically-derived MARSWIT dataset, within the high to low uncertainty limits. Because of this, confidence is relatively high for results as applied to Titan.

6.4 Titan Projections for Specific Conditions

The Titan results set utilized initial velocity conditions from Run 21M, which meant x-direction velocity was 0.4437 m/s and y-direction initial velocity was 0.3501 m/s. Despite this specific velocity condition, Figures 6.10 to 6.19 show the parametric variation in the properties of a Titan Average Particle (TAP) given by Dr. Burr, as listed below, in expected average flow:

Size Variation: *10, 180, 1000 microns*

Density Variation: *500, 1000, 1500 kg/m^3*

Phi Variation: *0.6, 0.9, 1.0*

Airspeed: *1, 2, 3 m/s*

Because FLUENT was not able to converge on any solutions for 1.0 m/s, 1.35 m/s test section velocity is the lowest presented for Titan. The 2 m/s case converged at 2.08 m/s and the 3 m/s case converged at 2.98 m/s.

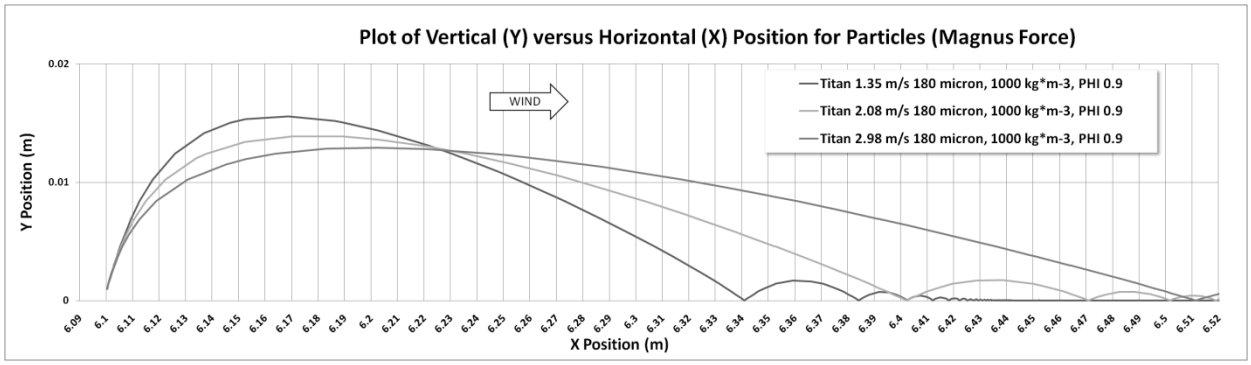

Figure 6.11: Titan Average Particle (TAP) Position versus Speed.

Figure 6.11 represents the reference plot for all other plots showing the TAP, below. To reduce confusion, it is shown only once, but its reference particle data is shown in each figure while varying the other parameters. The reference particle is 180 microns, 1000 kg/m^3, and Phi = 0.9. When a property is not being analyzed, its default value is the reference particle value.

Titan Size Variation:

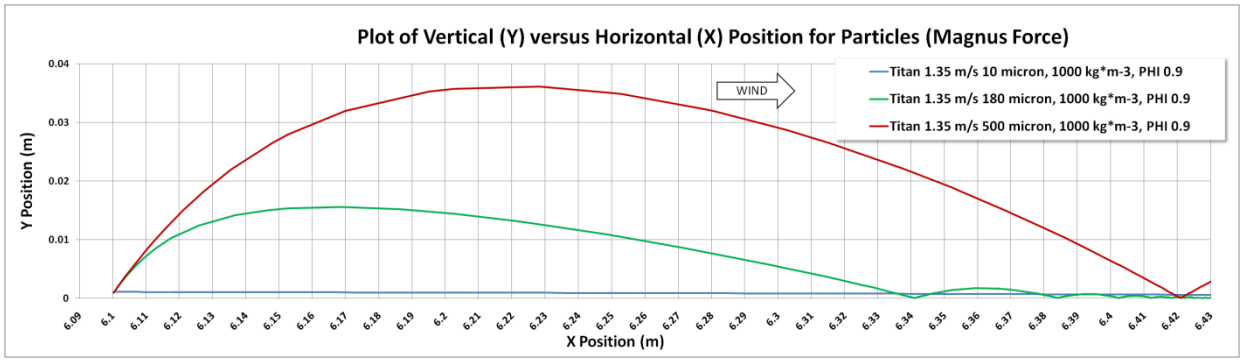

Figure 6.12: Titan Particle Size Variation versus TAP Position Plots, 1.35 m/s.

Figure 6.12 begins the size variation and shows relatively slow flow, at 1.35 m/s. The 10 micron particle lofts lower but does not enter true saltation, compared to the reference particle and the 1000 micron diameter particle. A possible reason for this could include a ballistic and drag effect, where the reduced size (and inertia) as compared to the other particles was not large enough to counteract the drag from a dense Titan atmosphere. Possible explanations for the long path length could include turbulence effects that maintain the small particle above the boundary layer.

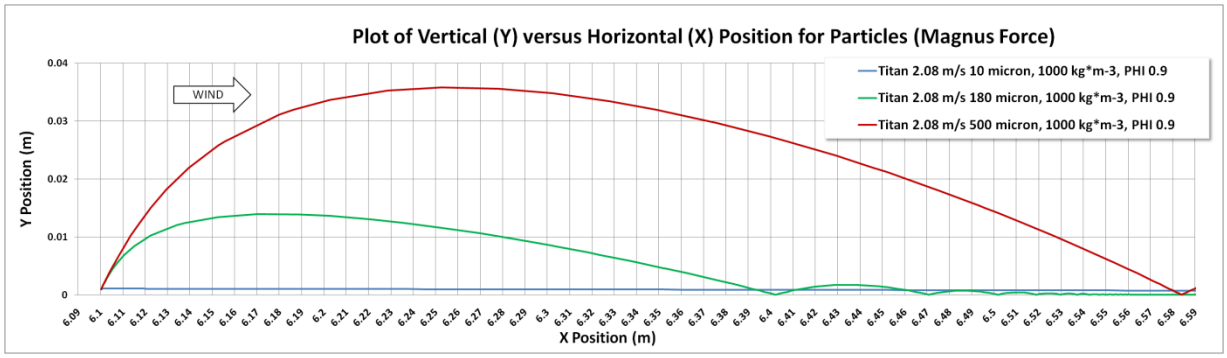

Figure 6.13: Titan Particle Size Variation versus TAP Position Plots, 2.08 m/s.

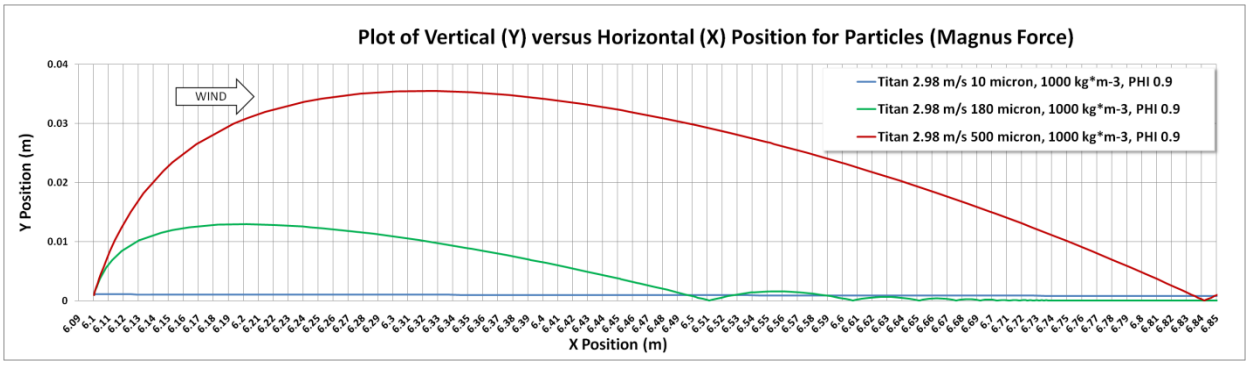

Figure 6.14: Titan Particle Size Variation versus TAP Position Plots, 2.98 m/s.

Density Variation:

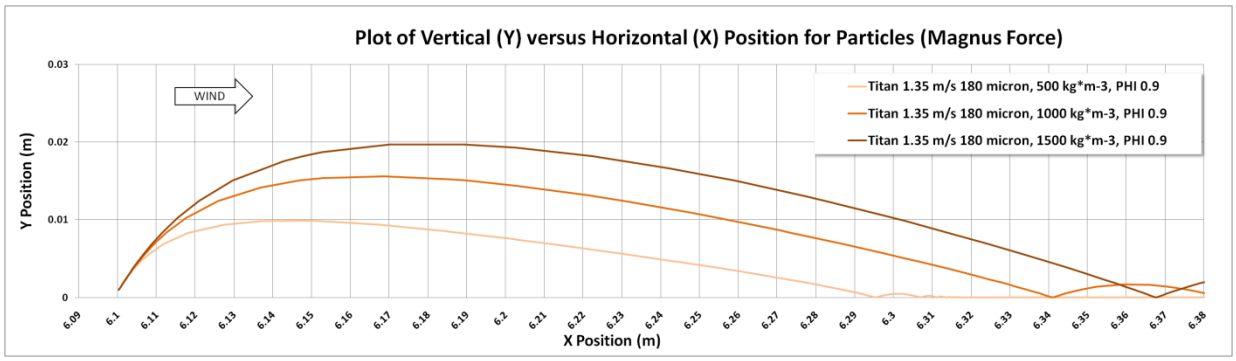

Figure 6.15: Titan Particle Density Variation versus TAP Position Plots, 1.35 m/s.

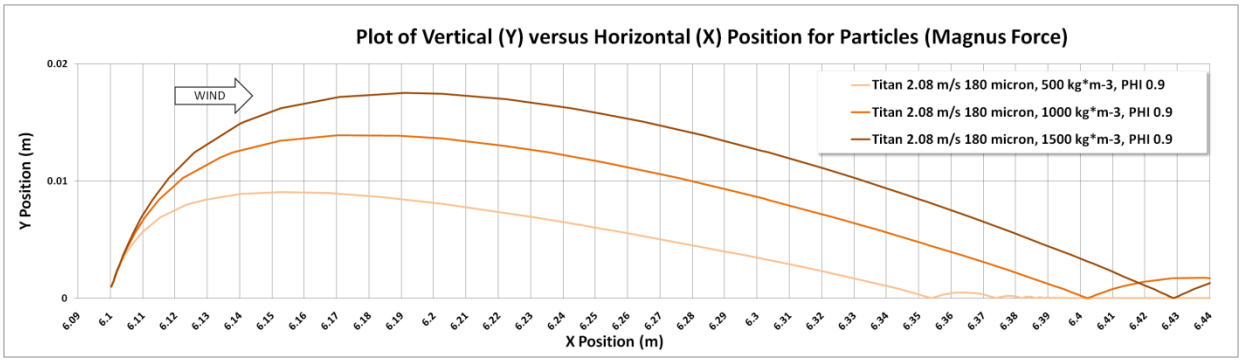

Figure 6.16: Titan Particle Density Variation versus TAP Position Plots, 2.08 m/s.

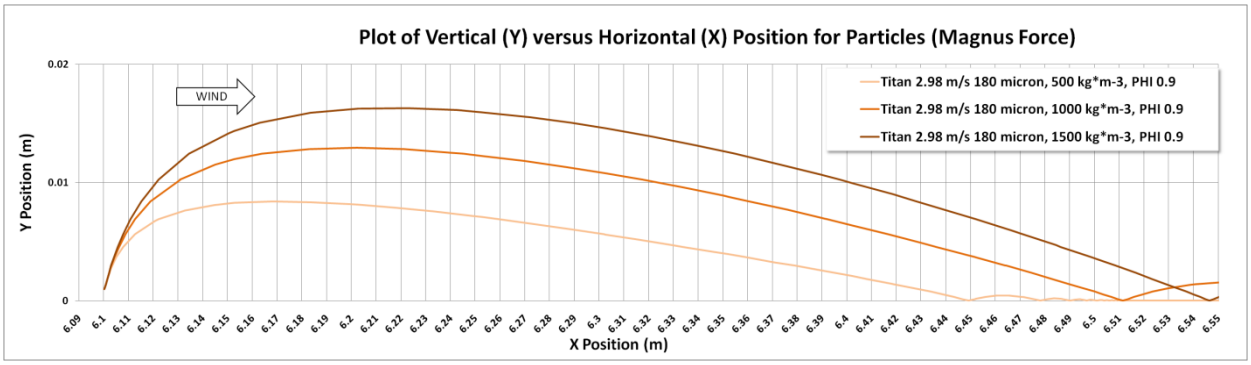

Figure 6.17: Titan Particle Density Variation versus TAP Position Plots, 2.98 m/s.

Figures 6.14 to 6.16 show density variation, and overall, the trajectory lofts are lower than when size was the varying parameter. The highest lofts can be seen to be the densest particles, which is reasonable, considering size is being held constant at its reference value of 180 microns.

PHI Variation:

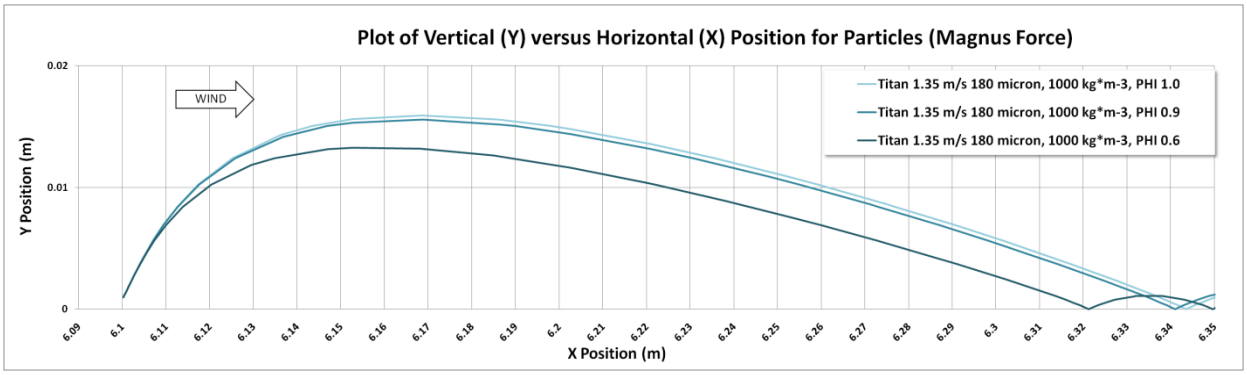

Figure 6.18: Titan Particle Phi (ϕ) Variation versus TAP Position Plots, 1.35 m/s.

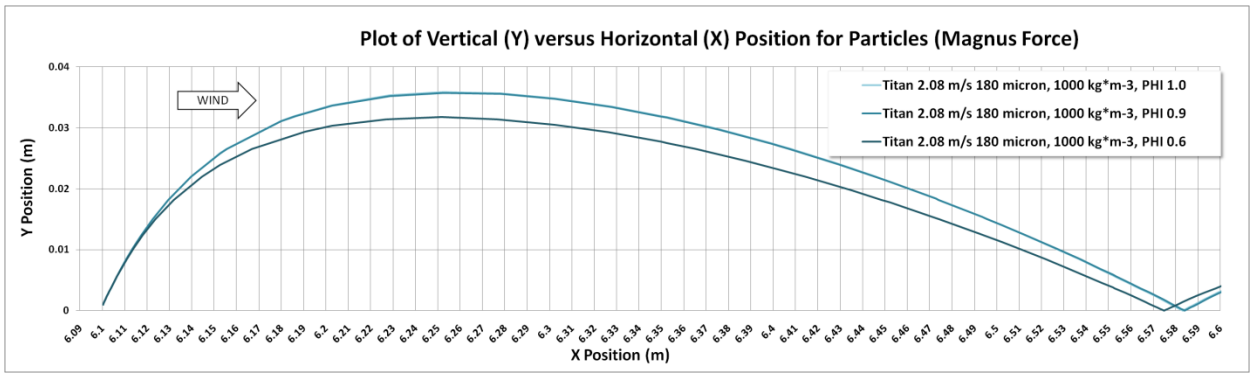

Figure 6.19: Titan Particle Phi (ϕ) Variation versus TAP Position Plots, 2.08 m/s.

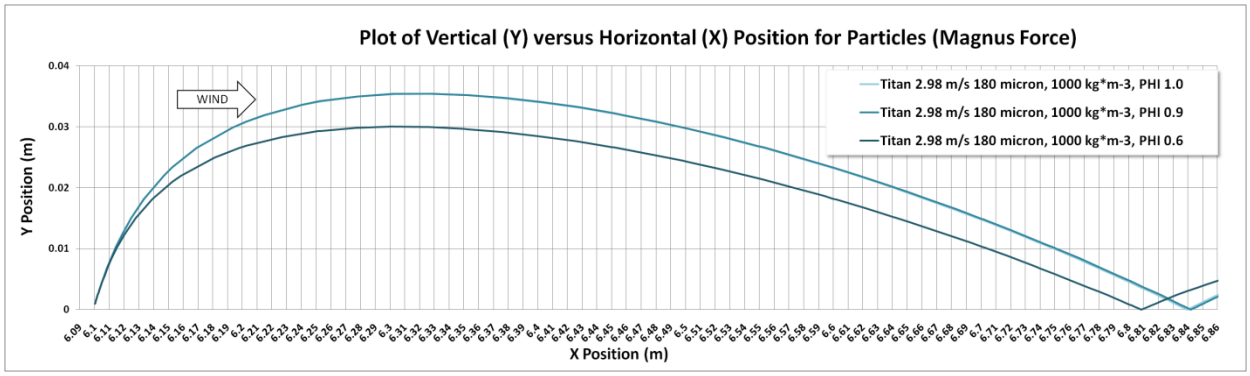

Figure 6.20: Titan Particle Phi (ϕ) Variation versus TAP Position Plots, 2.98 m/s.

There is very little difference between the Phi results for 1.0 and 0.9, but marked variation when Phi is reduced to 0.6. In general, loft heights for Titan particles exist in the 0.015 to 0.035 m range, and size and Phi variation results in the highest lofts. With increasing airspeed, one can see a direct correlation to substantially increased pathlengths. A comparison of ratios shows most height to length ratios for Titan results fall between a low and high value of 0.00579 and 0.1125, with an average value of 0.04856.

Table 6.1: Saltation Height to Length Ratios.

Saltation Height to Length Ratio			
Figure	Low	High	Average
6.11	0.03170	0.06250	0.04710
6.12	0.00579	0.11250	0.05914
6.13	0.00579	0.07423	0.04001
6.14	0.00579	0.04865	0.02722
6.15	0.05128	0.07407	0.06268
6.16	0.03529	0.05151	0.04340
6.17	0.02286	0.03371	0.02829
6.18	0.05909	0.06531	0.06220
6.19	0.06737	0.07423	0.07080
6.20	0.04225	0.04730	0.04478
Total Average			**0.04856**

6.5 Predicted Constant Spin Rates Required versus Relative Velocity

At a certain point, with respect to the particle of interest, there is varying relative velocity that, if increased sufficiently, reduces the applied gravitational acceleration in FLUENT to a point where, as far as FLUENT is concerned, there is zero gravity. If sufficiently high in real flows, these spin rates could cause particles of any size to create enough lift to suspend themselves temporarily on *Magnus force alone*. While these types of *constant* spin rate situations do not occur in viscous flows due to fluid friction, it is interesting to see how, if, having continued application of previous methodology from constant Magnus force correction, one can see where temporary particle suspension conditions might occur.

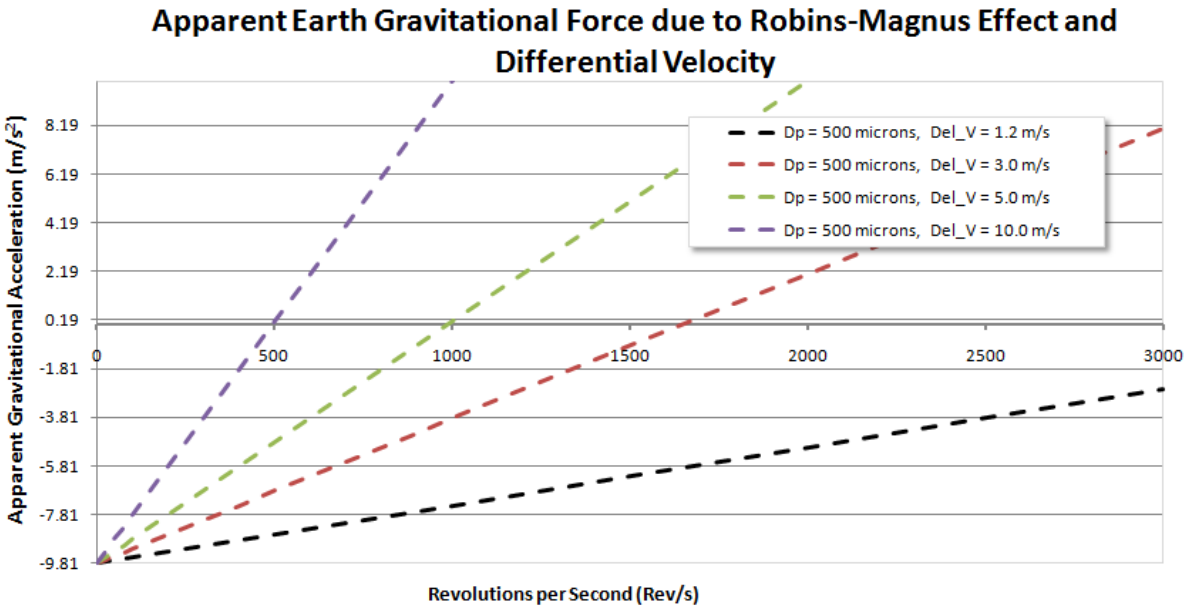

Figure 6.21: Apparent Earth Gravitational Force due to Magnus Force and Differential Velocity.

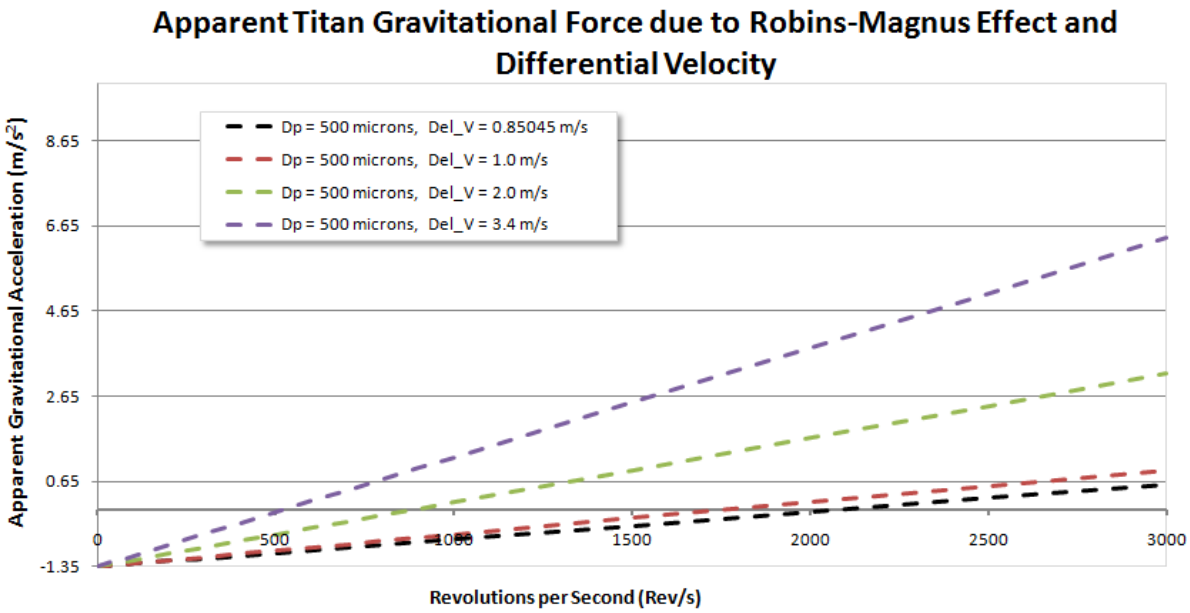

Figure 6.22: Apparent Titan Gravitational Force due to Magnus Force and Differential Velocity.

A potentially interesting projection made in Figure 6.22 is that, for a 500 micron particle at TAP density, suspension on Titan at 500 rev/s could occur at as little as 3.4 m/s differential velocity.

6.6 Predicted Static Threshold Friction Speed for Titan

Trajectories on Titan are unknown presently, but are estimated to be shallower and longer, with a higher minimum threshold speed than on Earth, due to the increased atmospheric pressure and reduced effect of gravity, as compared to the upper and lower bounds set by Venusian [31] and Martian simulation [30]. Particle diameters for Titan minimum threshold wind speed, estimated to be approximately 100 microns, are much larger than Earth's value of ~75 microns [12].

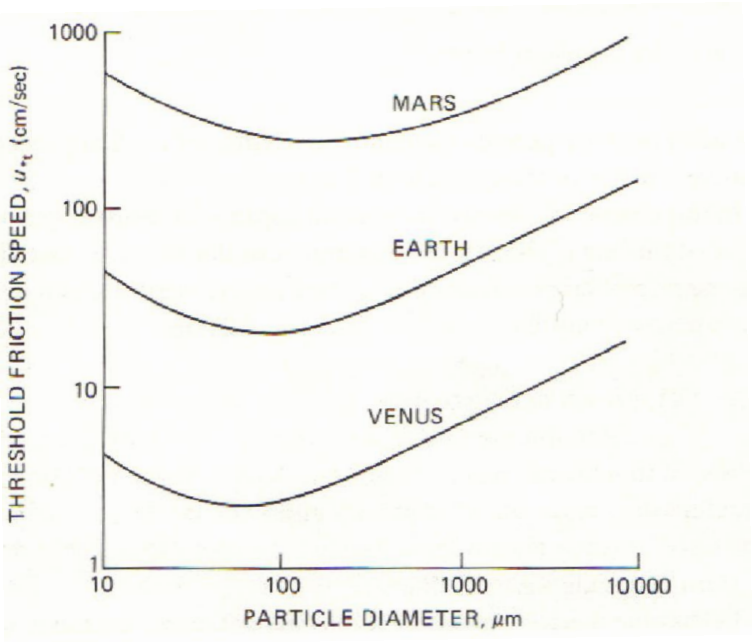

Figure 6.23: Threshold Friction Speed versus Particle Diameter for Different Planetary Bodies. [12]

By using a pressure equivalence equation below, based on relative wind velocity, one can calculate the wind speed required to produce the equivalent dynamic pressure on an identical particle. Particle size for Figure 6.24 was made to be 213 microns for both Earth and Titan particles. Where Cp = 1, and ρ values for each location are as defined earlier, the pressure equivalence equation is $P_1 = P_2$ or:

$$\frac{1}{2}\rho V_1^2 C_p = \frac{1}{2}\rho V_2^2 C_p \qquad (6.1)$$

V_1 is the Earth velocity at in MARSWIT at 6.45 m/s, and after solving, V_2 Titan velocity becomes as estimated 3.1 m/s. If read values from the fluid threshold speed for Earth in Figure 6.22, new estimates for Titan reduce threshold friction speed to the curve shown below. Minimum particle size for threshold continues to be approximately is 75-100 microns, but threshold friction speed is between Earth's and Venus's curves.

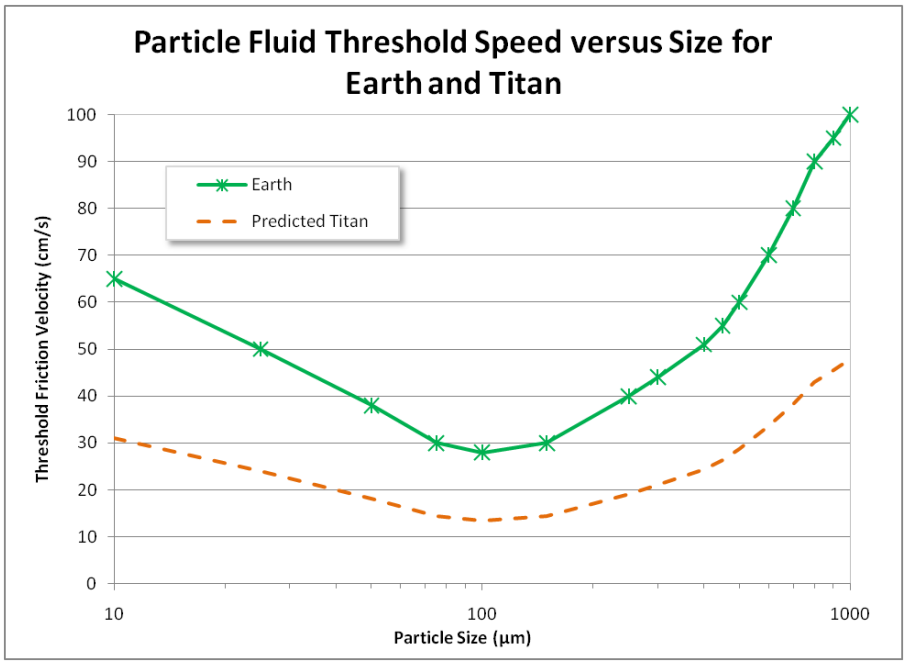

Figure 6.24: Particle Fluid Threshold Speed versus Size for Earth and Titan.

Results for identical particles were plotted for 6.45 m/s and 3.1 m/s for Earth and Titan cases, respectively, in Figure 6.25 below. The Titan loft arcs more than three to four times higher than the same initial force conditions for Earth. This is principally explained due to the comparatively low gravity, as compared to Earth, on Titan. Kok [35], in internal correspondence, comments Titan particles might be expected to have lower, shallower lofts as compared to Earth, but with longer pathlengths in general. In this thesis, the results indicate that, for equivalent forces, Titan particle fly up to four times higher and up to eight times longer.

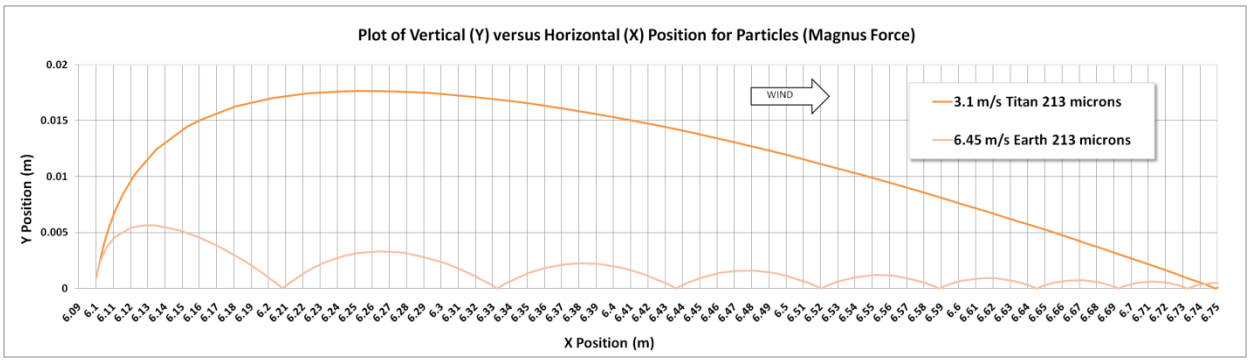

Figure 6.25: Comparison for Identical Earth and Titan Particles at Equivalent Initial Forces.

In summary, results shown demonstrate good trajectory correlation for the MARSWIT tunnel by falling near the uncertainty bounds established for each run. Because of the agreement and verification of those cases studied, Titan projections were calculated for varying parameters and shown. To facilitate the conceptualization of results for the two different environments, without the ability to reproduce static threshold friction speed, dynamic pressure equivalence from airspeed was determined for identical particles on Earth and Titan, and results show higher and longer lofts for Titan particles, at wind speeds of 3.1 m/s, which are within the nominal range of typical wind speeds there. So despite very specific results, it is likely results will be represented on Titan, and may be useful to future researchers.

Chapter 7

Uncertainty and Error Estimates

"In all science, error precedes the truth, and it is better it should go first than last."

– Hugh Walpole

7.1 Overview

Research at these slow wind speeds and relatively small particles introduced the possibility of large errors. Instrumentation for pressure measurement for the wind tunnel, resolution for the high-speed video, uncertainty in knowing the exact Phi or density for each particle, and having only four representative cases out of only 100 total chosen, all necessitate a careful discussion of error effects. Only four cases were chosen due to the complexity of tracking individual particles in flow and due to the conformance of the trajectory's paths to a single-bounce criterion.

7.2 Selection Bias

The first process the research team undertook once empirical data had been recorded at NASA Ames was to analyze the high-speed video data to select particles to verify in CFD. While ImageJ has add-on modules with automatic particle tracking, even that has visual detection thresholds that must be specified, and in our runs, human particle tracking was employed. Because of the relatively low resolution of the video data, approximately one pixel

per particle diameter, tracking a single, in-focus, particle was not trivial. Only when all conditions were ideal, and the particle was ejected from the creeping, rolling motion that was found near the floor, were the particles able to be followed. Some particles were too far into this chaotic environment, below which it was not possible to identify or track individual particles. Because of this, the research team chose the easiest particles to track, reducing the chance inter-particle collisions, or excessively turbulent flow near the particle, might have affected it; those isolated particles may not have been representative of the entire sample for each run.

7.3 Stochastic Effects

The particles used in typical two-phase studies vary wildly from each other, and, due to the small-scale nature of such flows and the multitude of different forces every particle undergoes, relatively small differences in any of the properties of a sample being tested can lead to unexpectedly large variation in results.

A number of other authors have contributed much in the field of particle, near-surface physics, and substantial literature exists to make testing and varying initial conditions for particles interacting with surface roughness effects, which were not modeled in this study. If good stochastic methods are available to describe the particle's or sample's range of trajectories or distribution due to shape factor, then they can be incorporated in the trajectory discussion in the future, since most surfaces include some roughness elements and natural diffusion of trajectories, which can and has been treated mathematically.

7.4 Small Particle Cohesive and Electrostatic Effects

Although FLUENT includes a body force term, it was not intended that Van der Waals forces, electro-magnetic or temperature-dependent inter-particle forces, fluidic bridging in voidage zones, and packing coefficients be modeled for different particle diameters. These forces do introduce effects on minimum static threshold, which other researchers associated with

the on-going Titan efforts are investigating. Because the model was not able to reproduce static threshold wind speed, this analysis was outside the scope of this thesis.

7.5 Spin Rate Value and Non-constant Spin Rate Effect

As mentioned earlier, body force corrections do not take into account the varying spin rate that real particles under-go in real flows. Due to viscous effects, particles shed energy into the local flow surrounding them as they spin, and will eventually stop spinning as they loft. If non-constant spin is taken into account, values for Magnus force correction would be correspondingly smaller toward the tail of each trajectory because of the reduction of angular spin velocity.

Also, the 500 rev/s value given by Kok and Loth seemed too high for naturally occurring spin in an atmosphere, but future research should focus on identifying a more accurate value for spin rates of small particles in viscous flow environments.

7.6 Density, Size, and Mass

The walnut shell particle property determination is subject to significant possible error. The imprecise nature of meniscus readings from measurement markings on a graduated cylinder, possible air bubbles on the surface of the crushed walnut shells sections (although care was taken to select a fluid with low surface tension), and accuracy of the mass balance all contribute some error. Below is Table 7.1 which presents the high and low variation for error in the density calculations accomplished.

Table 7.1: High and Low Variation for Walnut Shell Density Determination.

Particle Density (kg/m^3)					
High	1432	1497	1451	1384	1219
Low	851.2	890.0	862.8	822.4	886.9
High var.	363.0	378.7	367.3	351.0	192.0
Low var.	217.8	228.0	221.2	210.6	140.1

The average of the high density values above is the value used in the thesis results (1397 kg/m^3), when high density is required. Low density average (867.2 kg/m^3) is used accordingly, when required. Variation is calculated as the difference between each run's individual high and low values. The variation for each run was a result of the error of ±0.01 grams in the mass balance and ±0.5 mL between graduations in the volume measurements.

7.7 Noise in Data

Because of the low resolution in some instances of data recorded, there appeared to be noise (manifested as "steps") in what is typically a physically smooth ballistic trajectory for the particles. The curve-fit discussed earlier attempted to compensate for the step pattern discerned in the data, due to the low resolution the research team encountered in the original data from the high speed video.

7.8 Summary

In conclusion, the error bounds in our methodology and results included our projections and verified that MARSWIT results were reproduced, so Titan results proceeded apace from that conclusion. Notwithstanding, from the initial collection of data at NASA Ames (which could benefit from more precise local velocity determination for the tunnel), to the analysis of particles at the microscopic level, to the correction of Magnus lift in FLUENT, improvements remain to be made to reduce error and increase confidence in the results. Increasing number of runs analyzed, increasing video resolution, and predicting an accurate value for the coefficient of restitution (as a result of bed interaction) all contribute to reducing error. The nature of empirical data collection is difficult at these sizes and numbers of particles, and limitations in FLUENT CFD code make an interpretation of results a study in tradeoffs and benefits. Results with COMSALT may provide increased accuracy with reduced error, as some of these factors are explicitly addressed through MATLAB.

Chapter 8

Summary and Future Work

Science is a wonderful thing if one does not have to earn one's living at it.

– Albert Einstein

8.1 Summary and Review of Thesis

Preliminary data of Titan from the NASA Cassini-Huygens mission indicate there is evidence of a dynamic environment, including aeolian dune formation, and potential large-scale surface transport processes, examples of which are on-going topics of research for Earth, Mars, and Venus.

While it is in our interest to model particle dynamics in wind tunnels due to the reduced cost as compared to space probes (or even manned expeditions), it has long been a challenge to accurately measure small scale movement of sediment. This research demonstrated a numeric modeling technique for Titan will simplify much of this work, and allow the researcher the ability to model dynamically similar effects to those seen on Earth. If time is taken to collect basic data on differing atmospheres and particles in the solar system, then the immediate benefit realized is demonstrably accurate simulation of planetary body surface particle dynamics at considerably less cost than operating a wind tunnel, optimizing and planning multiple flybys for a spacecraft, or having rovers descend to the surface.

While it is of great interest to model particle dynamics in wind tunnels due to the reduced cost as compared to space probes (or even manned expeditions), it has long been a challenge to

accurately measure small scale movement of sediment. Care must be taken to reduce error wherever possible.

In conclusion, FLUENT provides a good first-order approximation of particle-flow dynamics, with a good CFD-empirical correlation found for MARSWIT tunnel data. Titan predictions show high and long particle trajectories at very low threshold wind speeds, lower than those of Earth for similar particle sizes.

8.2 Future Work

Future research goals include expanding the model to validate TWT data in conjunction with the team working at NASA Ames, eventually simulating dune formation and other aeolian processes on any planetary body of interest. The current code was able to reproduce results that match well with the current data, given a calculated initial velocity condition, but it should be possible to use FLUENT in the future to "self-generate" the static threshold friction speed (μ_{*_t}) and initial saltation velocities for a given particle within a flow field in fully-developed turbulent condition through natural shear and viscous lift forces. Additionally, the code is capable of determining flux rates for discrete particles through surfaces oriented in the normal direction to the flow at specific heights. Therefore, it is proposed that FLUENT be used in the future to generate data on particulate flux to compare to MARSWIT trap samples.

Aside from a correct model of the flow field, the most important single factor needed to accurately calculate particle trajectories is a reliable value of the coefficient of drag. This value depends critically on both the Reynolds number and on the shape of the particle; subsonic drag coefficients can vary by well over an order of magnitude. To further ensure that our computational model is generating results that are consistent with the experimental data, it may be possible to evaluate each particle tested in MARSWIT microscopically before releasing it into saltation, to determine an average value and standard deviation of the shape factor described above with known particles and their specific trajectories.

The current methodology for the model and simulation did not lead to self-generated static threshold friction speed, however it could have been that the GAMBIT mesh was actually

overly-refined and was smaller than what FLUENT expected, compared to the size of the tested particles. The static threshold speed limitation could also be a model issue with respect to the roughness height impinging the lower levels of the mesh nodes, which in turn could have created numerical instabilities. Though the solution converged in most cases, unless an initial value for (at a minimum) y-component velocity was dictated, then the particle did not generate normal lift to the floor at any speed. Once additional focus is applied to this particular challenge, it is likely that the mesh model can be re-calibrated to generate the data from more versatile initial conditions. Preliminary results using extra-coarse meshes in idealized tubes under similar flow conditions and particles yielded encouraging lift-off trajectories with no initial velocity input.

The final point of consideration would include eventual discussion and investigation into the coefficient of restitution for FLUENT's use. This, for walnut shells, would have to be determined experimentally, much like the process for density of the shells. The eventual aim of such a determination would be to refine the predicted values for trajectories *after* a bounce on a surface or with other particles in a packed bed, and it would be worthwhile to include discussions of stochastic effects, although this may mean a MATLAB model would have to be preferred.

In the end, FLUENT provided a good first-estimate of highly uncertain conditions on Earth, and results for Titan demonstrate preliminary expectations of what may possibly be occurring on the surface. As long as Titan data and surface processes remain unknown unknowns, researchers can only make the best possible educated guesses until new robotic or (preferably) manned missions to Titan are funded and carried out.

List of References

1. Abramoff, M.D., Magelhaes, P.J., Ram, S.J. Image Processing with ImageJ. Biophotonics International, volume 11, issue 7, pp. 36-42. 2004.
2. Allen, J.R.L. Fundamental properties of fluids and their relation to sediment transport processes. In Pye, K. (ed.), Sediment Transport and Depositional Processes. Blackwell Scientific Publications: Oxford, Chapter 2, pp. 25-60. 1994.
3. Almeida, M. P., et al. Aeolian transport layer, Phys. Rev. Lett., 96(1), 018001, doi:10.1103/PhysRevLett.96.018001. 2006.
4. Almeida, M. P., et al. Giant saltation on Mars, Proc. Natl. Acad. Sci. U. S. A., 105(17), 6222– 6226, doi:10.1073/pnas.0800202105. 2008.
5. Anderson, John D. Fundamentals of Aerodynamics. Fourth Edition. International Edition. 2007.
6. Bagnold, R.A. The Physics of Blown Sand and Desert Dunes. Methuen, London. 1941.
7. Baker, A.J. The Computational Engineering Sciences. The University of Tennessee CFD Laboratory Press. 2006.
8. Bansal, R. K., Walker, J. T., and Gardisser, D.R. Validating FLUENT for the Flow of Granular Materials in Aerial Spreaders, Transactions of the ASAE, Vol. 41 (1): 29-35.
9. Bradshaw, P., Cebeci, T., and Whitelaw, J.: Engineering and Calculation Methods for Turbulent Flow. Academic Press, New York. 1981.
10. Cebeci, T. and Bradshaw, P. Momentum Transfer in Boundary Layers. Hemisphere Publishing Corporation, New York. 1977.
11. Crane Company. Flow of fluids through valves, fittings, and pipe. Technical Paper No. 410 (TP 410). 1998.
12. Greeley, R., Iversen, J. D. Wind as a Geological Process on Earth, Mars, Venus and Titan. Cambridge Planetary Science Series no. 4. Cambridge, London, New York, New Rochelle, Melbourne, Sydney. Cambridge University Press. 1985.
13. Greeley, R., Marshall, J.R., and Leach, R. N. Microdunes and other aeolian bedforms on Venus: wind tunnel simulations. Icarus 60, 152-160. 1984b.
14. Greeley, R., Leach, R. N., White, B., Iversen, J., and Pollack, J. Threshold windspeeds for sand on Mars: wind tunnel simulations. Geophys. Res. Lett. 7(2), 121-124. 1980.
15. Haider, A., Levenspiel, O. Drag Coefficient and Terminal Velocity of Spherical and

Nonspherical Particles. Powder Technology 58(1): 63-70 May 1989.

16. Iverson, J.D., Greely, R., Pollack, J. B., and White, B. R. Simulation of Martian eolian phenomena in the atmospheric wind tunnel. *Space Simulation*, NASA Spec. Publ. SP-36, 191-213. 1973.
17. Kok, Jasper F. and Renno, Nilton O. A comprehensive numerical model of steady state Saltation (COMSALT). 2009.
18. Launder, B. E. and Spalding, D. B. The Numerical Computation of Turbulent Flows. Computer Methods in Applied Mechanics and Engineering, 3:269-289. 1974.
19. Lorenz, R. What Titan is really like: In-situ measurements of the Titan environment by the Huygens probe. IEEE Aerospace Conference Proceedings [1095-323X]. 2006.
20. Losenno, C. and Easson, W. J. Free-falling of irregular particles. 4th Int. Conference of Multiphase Flow, New Orleans, ICMF. 2001.
21. Loth, E. Lift of a solid spherical particle subject to vorticity and/or spin, AIAA J., 46(4), 801– 809, doi:10.2514/1.29159. 2008.
22. Mell, B. Topography and Roughness Testing of Sandpaper Surface. http://www.nanovea.com/Application%20Notes/SandPaper.pdf. Nanovea Company. 2010.
23. Pollack, S. R., Meaney, D. F., Levine, E. M., Litt, M., Johnston, E. D. Tissue Engineering. October 2000, 6(5): 519-530. doi:10.1089/107632700750022161.
24. Radebaugh, J. et al. Longitudinal Dunes on Titan as indicators of global climate. Workshop on Ices, Oceans, and Fire: Satellites of the Outer Solar System VOL ISSU PAGE 114-15 DATE Aug. 2007 Lunar and Planetary Institute, Houston, TX, USA. 2007.
25. Morsi, S. A. and Alexander, A. J. An Investigation of Particle Trajectories in Two-Phase Flow Systems. J. Fluid Mech., 55(2): 193-208, September 26 1972.
26. Tomasko, M.G., and 39 colleagues. Rain, winds, and haze during the Huygens probe's descent to Titan's surface. Nature 438, 765–778. 2005.
27. Tsuji, Y., Shen, N. Y., and Morikawa, Y. Numerical simulation of gas-solid flows I: Particle-to-wall collisions. *Tech. reports of Osaka University*, Vol. 39, pp. 233-241. 1989.
28. Wadell, H. *J. Franklin Inst.* (April 1934), p. 459. 1934.

29. White, B.R., Greely, R., Iverson, J.D., and Pollack, J.B. Estimated grain saltation in a Martian atmosphere. *Journal of Geophysical Research* 81 (32), 5643-50. 1976.
30. White, B.R. Soil transport by winds on Mars. *Journal of Geophysical Research* 84, 4643-4651. 1979.
31. White, B.R. Venusian Saltation. *Icarus,* Volume 46, No. 2. Academic Free Press, May. 1981.
32. White, Frank M. Viscous Fluid Flow. Third Edition, McGraw-Hill International Edition, New York. 2006.
33. White, Frank M. Fluid Mechanics. Fourth Edition, McGraw-Hill, New York. 1999.
34. Fluent User Documentation. http://my.fit.edu/itresources/manuals/fluent6.3/help/html/ug/node1.htm.
35. Internal correspondence, J. Kok and author of thesis.
36. Internal correspondence, J. Hills and author of thesis.

Vita

Oscar Mathews was born in Madrid, Spain and graduated from the US Air Force Academy before attending The University of Tennessee, Knoxville. He has a younger brother, Anthony Mathews, and his parents David and Pilar Mathews, all of whom live in Memphis, TN. While at the US Air Force Academy, Oscar earned his Bachelor's of Science in Aeronautical Engineering and Private Pilot's License. He served honorably as an officer before separating as a Captain, and before leaving the Air Force, Oscar completed a six month tour in Kuwait. Oscar loves motorcycles, aircraft, playing the trumpet, and hopes one day to have the opportunity to explore space and (especially) Titan.